Vertical-axis wind turbine aerodynamics

De Tavernier, D.A.M.; Ferreira, Carlos; Goude, Anders

DOI
10.1007/978-3-030-05455-7_64-2

Publication date
2022

Document Version
Final published version

Published in
Handbook of Wind Energy Aerodynamics

Vertical-Axis Wind Turbine Aerodynamics

Delphine De Tavernier, Carlos Ferreira, and Anders Goude

Contents

D. De Tavernier (✉) · C. Ferreira
Department of Aerospace Engineering, Delft University of Technology, Delft, Netherlands
e-mail: D.A.M.DeTavernier@tudelft.nl; c.j.simaoferreira@tudelft.nl

A. Goude
Department of Electrical Engineering, Uppsala University, Uppsala, Sweden
e-mail: anders.goude@angstrom.uu.se

B. Stoevesandt et al. (eds.), *Handbook of Wind Energy Aerodynamics*,
https://doi.org/10.1007/978-3-030-05455-7_64-2

Abstract

Horizontal-axis wind turbines (HAWTs) are widely studied and have proven their technological capabilities. However, wind turbines are moving into new environments, such as floating far-offshore or urban applications, where the operational conditions are significantly different. Vertical-axis wind turbines (VAWTs) could be more suitable and compatible in these environments, hence, the interest in VAWTs is rekindling. Although vertical-axis wind turbines have a long history, the behavior of these turbines and their complex flow field is still not fully understood. The lack of understanding the complex unsteady aerodynamics of VAWTs and the challenge to predict the loads and performance of this kind of turbines accurately, has led to systematic failures and as such variable interest in VAWTs throughout history. Advancing the understanding and modeling of VAWT's aerodynamics will be crucial to advance the technology further.

This chapter highlights the main aerodynamic phenomena and challenges of vertical-axis wind turbines. First, an introduction is provided on the VAWT history and (dis-)advantages. The basics of VAWT aerodynamics and the various rotor simplifications/representations are presented. Further, the state-of-the art aerodynamic modeling techniques, specifically for VAWTs, are discussed. Since VAWTs are inherently unsteady, the main unsteady phenomena that play a crucial role in VAWT aerodynamics are summarized. Finally, wake aerodynamics and the importance of airfoil design for VAWTs are highlighted.

Keywords

Vertical-axis wind turbine · VAWT · Rotor and wake aerodynamics · Unsteady aerodynamics · Aerodynamic modelling

Introduction

History of VAWTs

Wind turbines have a very long history. The earliest known wind powered grain mills and water pumps were used by the Persians in the years 500–900. In fact these wind turbines were vertical-axis turbines. The ancient windmills were made out of clay, straw, and wood and have been used to mill grain for flour.

Drag-driven vertical-axis wind turbines have been around for centuries in one form or another, including the well-known design of Savonius in 1922. They typically have rounded paddles with a convex shape. This allows a difference in drag between the leeward and windward parts of the rotation, resulting in a positive work. A drag-driven turbine typically has a limited efficiency (power coefficient below 0.3) but presents advantages on self-starting and higher power output at low wind speeds. The 3D drag-driven turbine comes in different shapes, often with helical or straight blades. Also the amount of blades/paddles differs.

The lift-driven VAWT, as its HAWT counterpart, relies on lift for the generation of torque, with a component of the lift force directed in the rotational direction. The first patent of a lift driven VAWT was by Darrieus in 1931. The original concept of Darrieus is the Φ-shaped rotor. An advantage of this shape is that the blades are constantly in tension, in principle allowing for better structural performance and lighter blades. Another conventional lift-driven design is the H-shaped rotor. This rotor has straight blades connected by struts to the shaft. Other rotor shapes have been developed, from V-rotors to H-rotors with helical blades. The final result of all the different rotor shapes is to create a 3D actuator surface that is cylindrical (rectangular, conical, ellipsoidal), where the streamtubes are acted upon by multiple regions of the actuation surface, generated by the blades or struts.

Because of the oil crisis in the 1970s and the beginning of the 1980s, wind energy research accelerated, with a new period of experimentation with different concepts of horizontal- and vertical-axis wind turbines. The developments in these golden years resulted in commercial turbines, for example, FloWind. FloWind installed more than 500 vertical-axis turbines in California and in 1987 they represented a total capacity of around 100 MW. The simpler aeroelastic and fatigue behavior of the HAWT for scales below 10 MW resulted in a faster technology development of the HAWT vs the VAWT. HAWTs reached technological maturity and became the dominant concept in the market.

Although the gap between VAWTs and HAWTs is nowadays wider than ever, there is a renewed surge of interest in VAWTs. The interest in VAWTs is growing again, driven by two scales of application for which HAWTs tend to underperform: the small-scale turbines in high turbulence environment (e.g., urban environment) and >20 MW (floating) offshore wind energy. The challenge of offshore wind combined with upscaling raises the question whether other concepts such as vertical-axis wind turbines could be more suitable and allow a reduction in the cost of energy.

Fig. 1 presents a timeline of the development of VAWTs (above 100 kW) that were built, including both experimental turbines, prototypes, and commercial models produced in larger numbers. The two phases of VAWTs can easily be recognized: one around the 1980–1990s and one coming up in the last decade. Also, in the 2010s, there has been a revival for the H-rotor concept while in the past the Φ-

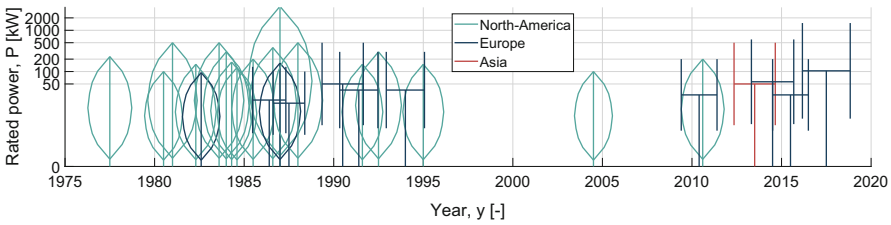

Fig. 1 Timeline VAWTs larger than 100 kW. This figure is based on the work of Möllerström et al. (2019)

rotor was preferred. Finally, the timeline also shows a geographical shift on where these developments occur (Borg et al. 2014; Möllerström et al. 2019; Kumar et al. 2019).

Some relevant VAWT case studies are worth mentioning. The *Magdalen Island* turbine installed in 1977 was one of the first turbines sparking the first revival of the VAWT around the oil crisis. The Darrieus turbine *Éole* was installed in 1987 in Quebec in Canada and had a total height of 110 m. The rated power of this turbine was 3.8 MW and till today is the largest VAWT ever constructed. The strut-free *Sandia 34 m turbine* is the most tested and studied design, and a case study for model development. *Pionier I* was a VAWT concept installed on a floating platform in Amsterdam, decommissioned in the beginning of the 1990s. The *T1-turbine* (developed by Vertical Wind currently owned by Uppsala University in Sweden) is one of the first turbines sparking the second revival. It is a 200 kW turbine and had an aerodynamic power coefficient measured to be 0.33. Finally, the 1.5 MW Polish *Anew-B1* turbine is the second largest turbine regarding both power and swept area and the largest H-rotor ever build in history.

Advantages and Disadvantages Between HAWT and VAWT

The comparison between HAWT and VAWTs is often described as a list of advantages and disadvantages. However, such list often does not account for the full range of design options of both concepts. With this section we aim to add some detail to the discussion.

One of the potential advantages is that VAWTs create a cylindrical actuation surface that can be perceived as omnidirectional. This means that the actuation surface is always perpendicular to the flow direction and, in principle, the VAWT does not suffer from yaw misalignment. However, active load/circulation control on a VAWT will require azimuthal/yaw awareness. Azimuthal update is faster and more robust than yaw alignment, resulting in less power loss and fatigue.

Another potential advantage is that because the rotating axis is vertical to the ground, the heavy electrical components can be located close to the ground. This causes the maintenance to be easier and to lower the center of gravity. This is beneficial for floating applications (Griffith et al. 2016). However, VAWTs tend to operate at lower tip speed ratios, resulting in larger torque, impacting the drive train. Turbines rotating slower produce less noise.

Preliminary studies have pointed out that VAWTs are easier to scale up than HAWTs (Sutherland et al. 2012), resulting in lower turbine costs for concepts larger than 20 MW. The challenge for VAWTs then becomes standstill load cases (Griffith et al. 2018), due to the three-dimensionality of the rotor.

VAWTs show a faster wake recovery and are more suitable for wake control due to the 3D actuation surface. A VAWT wind farm can have a smaller footprint, with turbines placed closer together and a higher power density per ground surface.

VAWTs are more challenging to design due to the unsteady 3D aerodynamics and resulting aeroelastic phenomena. Further in this chapter we aim to highlight

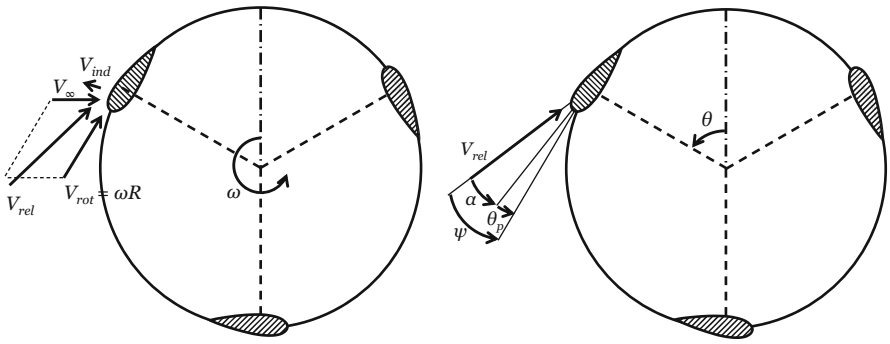

(a) Relative velocity (b) Angles

Fig. 2 Velocity vectors and angle definitions of a 2D blade element. (**a**) Relative velocity. (**b**) Angles. (Adapted from De Tavernier 2021)

key aerodynamic phenomena of VAWTs and modeling approaches that are often not addressed in literature.

Basic VAWT Aerodynamics

To understand the basic aerodynamic characteristics of a lift-driven VAWT, a 2D blade element can be considered. A rotor is defined by the radius R, chord c, and number of blade B. The blades have a length or span H and rotate at an angular velocity ω.

At the 2D blade element, as given in Fig. 2a, there are three velocity components acting on the blade when flying through the air. The first component is the incoming wind $\overrightarrow{V_\infty}$. The second component is caused by the rotational speed of the turbine. The rotational velocity $\overrightarrow{V_{\text{rot}}}$ is equal to the rotational speed ω times the radius of the rotor R. The third component is the induced velocity $\overrightarrow{V_{\text{ind}}}$. This induced velocity is caused by the presence of the forcefield created by the turbine inside the flowfield. The size of the induced velocity component varies over the rotation and depends on the thrust coefficient of the turbine and on the gradient of the force distribution over the actuator.

The relative velocity is given by Equation 1 and can be decomposed in any direction of interest. The velocity vector can be decomposed into the x- and y-direction, being the inflow and cross-flow direction, respectively. Also, the direction normal and tangential to the actuation surface (rotating blade path) can be considered. Here the normal velocity is defined positive when pointing in the counter-rotating direction. The tangential direction is positive when pointing inwards.

$$\overrightarrow{V_{\text{rel}}} = \overrightarrow{V_\infty} + \overrightarrow{V_{\text{rot}}} + \overrightarrow{V_{\text{ind}}} \tag{1}$$

and:

$$V_x = V_\infty + \omega R \cdot \cos(\theta) + V_{\text{ind},x}$$

$$V_y = \omega R \cdot \sin(\theta) + V_{\text{ind},y}$$

$$V_t = V_x \cdot \cos(\theta) + V_y \cdot \sin(\theta)$$

$$V_n = V_x \cdot \sin(\theta) - V_y \cdot \cos(\theta)$$

The angle of attack α, indicated in Fig. 2b, is the angle between the relative velocity vector and the airfoil chordline. The inflow angle Ψ is the angle between the relative velocity vector and the tangent of the rotational path. The pitch angle θ_p is the angle between the airfoil chordline and the tangent of the rotational path. The definitions and Fig. 2b reveal that the inflow angle is thus the sum of the angle of attack and pitch angle, as defined in Equations 2 and 3. It is common practice to define the azimuth angle θ as the angle between the cross-flow direction and the blade location. Therefore, the azimuth angle is between 0 and 180 degrees in the upwind part of the rotor and between 180 and 360 degrees for the downwind part of the rotor.

$$\alpha = \Psi - \theta_p \tag{2}$$

$$\alpha = \tan^{-1}\left(\frac{V_n}{V_t}\right) - \theta_p \tag{3}$$

Using a blade element approach, we determine the lift and drag force coefficients of the airfoil at given operational conditions. Multiplying the lift and drag coefficient with $0.5\rho V_{\text{rel}}^2$ and the chord c gives you the lift and drag force per unit span. The 2D lift force L_{2D} and drag force D_{2D} (per unit span) are perpendicular and in line with the relative velocity, as indicated in Fig. 3. These forces can be decomposed into a normal F_N and tangential F_T force (per unit span) using the inflow angle. A positive sign for a normal force corresponds to a vector pointing inwards and a tangential force in positive when in the rotating direction (from trailing edge to leading edge). Note that in literature other sign conventions might be used.

$$L_{2D} = \frac{1}{2}\rho V_{\text{rel}}^2 \cdot C_L(\alpha) \cdot c \tag{4}$$

$$D_{2D} = \frac{1}{2}\rho V_{\text{rel}}^2 \cdot C_D(\alpha) \cdot c \tag{5}$$

and:

$$F_N = L_{2D} \cdot \cos(\Psi) + D_{2D} \cdot \sin(\Psi) \tag{6}$$

$$F_T = L_{2D} \cdot \sin(\Psi) - D_{2D} \cdot \cos(\Psi) \tag{7}$$

Power is the rate of work by the force applied over a distance x. The average power over one revolution can be achieved by multiplying the rotational velocity ωR with the average tangential force. The average tangential force is equal to the integrated tangential force over one revolution, multiplied by the number of blades and divided by 2π. The average thrust of the system is the average x-force of all the blades over one revolution. Remember that the power coefficient C_P is the power of the turbine divided by the power available in the wind being $0.5\rho V_\infty^3 2R$. The thrust coefficient C_T is the thrust divided by $0.5\rho V_\infty^2 2R$.

$$P_{2D} = \frac{1}{2\pi}\int_0^{2\pi} B \cdot F_T(\theta) \cdot \omega R \cdot d\theta \tag{8}$$

$$T_{2D} = \frac{1}{2\pi}\int_0^{2\pi} B \cdot (F_T(\theta)\cos(\theta) - F_N(\theta)\sin(\theta)) \cdot d\theta \tag{9}$$

and:

$$C_P = \frac{P_{2D}}{0.5\rho V_\infty^3 2R} \tag{10}$$

$$C_T = \frac{T_{2D}}{0.5\rho V_\infty^2 2R} \tag{11}$$

The VAWT community typically uses the non-dimensional geometrical parameters rotor solidity and aspect ratio. The rotor solidity, typically indicated with σ, expresses the ratio between the platform area of the blades and the projected area of the rotor ($\sigma = \frac{Bc}{2R}$). The aspect ratio is the ratio between the blade length and rotor diameter ($AR = \frac{H}{2R}$). The relation between the rotational velocity at the blades and the freestream velocity is the tip speed ratio and referred to as λ ($\lambda = \frac{\omega R}{V_\infty}$).

Applying the equations on a 2D VAWT blade element results in Fig. 4. For a typical rotor without blade pitch, the angle of attack is varying over the cycle. In the

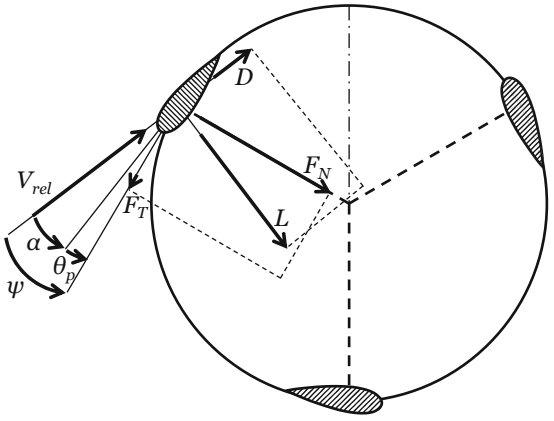

Fig. 3 Forces acting on a 2D blade element. (Adapted from De Tavernier 2021)

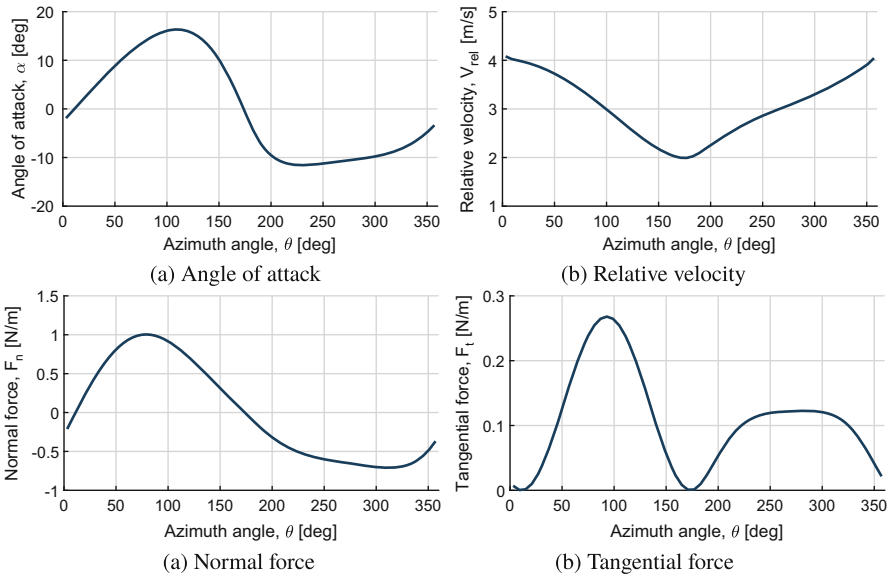

(a) Angle of attack (b) Relative velocity

(a) Normal force (b) Tangential force

Fig. 4 Operational conditions of a typical 2D VAWT blade element. Radius $R = 1\,\text{m}$, chord length $c = 0.1\,\text{m}$, number of blades $B = 2$, incoming velocity $V_\infty = 1\,\text{m/s}$, rotational speed 3 rad/s, lift polar $C_l = 2\pi \sin(\alpha)$, drag polar $C_d = 0$. (**a**) Angle of attack. (**b**) Relative velocity. (**c**) Normal force. (**d**) Tangential force. (Adapted from De Tavernier 2021)

upwind part of the rotor, the angle of attack is positive while downwind, the angle of attack is negative. The relative velocity at a zero azimuth angle is the largest since the incoming velocity and the velocity caused by the rotation of the turbine are in the same direction. At an azimuth angle of 180 degrees, the incoming velocity and rotational velocity are in the opposite direction and as such the relative velocity is minimum. The normal blade forces per unit span also vary over the cycle, positive upwind and negative downwind, with its maximum value at an azimuth angle around 90 degrees. The tangential force per unit span is mostly positive and thus pointing in the rotating direction. It is the largest for the upwind part. Note that this load distribution is the consequence of choosing a symmetric airfoil at zero pitch angle. Later in this chapter, we will address the effect of other configurations on the load distribution. How to achieve the induced velocity will be treated in section "VAWT Modeling Techniques".

Rotor Representations

For VAWT analysis, the rotor is often simplified. Commonly, there are four levels of VAWT representations, as summarized in Fig. 5.

The first level focuses only on the main torque-producing component, namely the rotor blades. All other components such as the struts or the tower are disregarded.

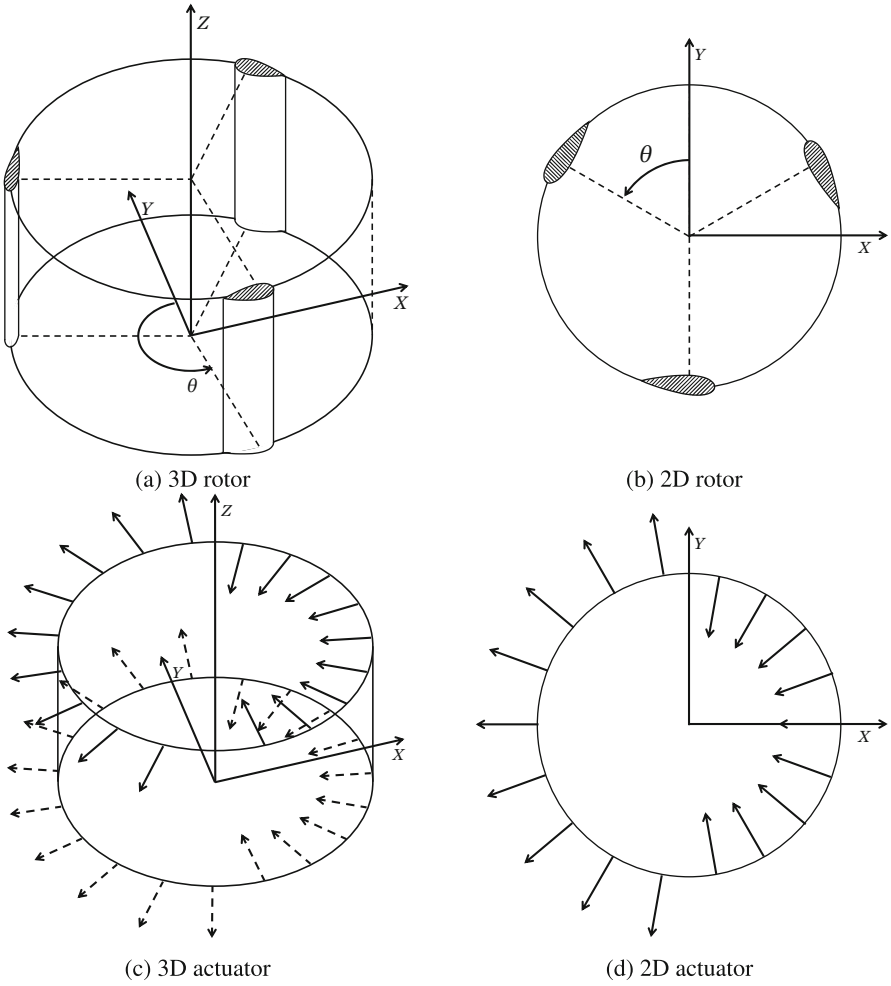

Fig. 5 VAWT simplification levels. (**a**) 3D rotor. (**b**) 2D rotor. (**c**) 3D actuator. (**d**) 2D actuator. (Adapted from De Tavernier 2021)

The 3D rotor considers the effect of finite number of blades and finite blade length. By isolating one slice of the 3D rotor, or by omitting the spanwise direction, the 2D rotor can be analyzed. In this rotor simplification, the finite number of blades is still considered; however, the blades are assumed to have an infinite blade length. No tip effects are included. In the third and fourth level, the 3D and 2D rotor are replaced by a 3D or 2D actuator surface. The actuator cylinder concept is an extension of the actuator disk concept (Madsen 1982). An actuation surface is introduced that coincides with the swept area of the rotor. In 3D, this is a cylinder; in 2D this is a circle. On the actuation surface you apply the reaction of the average blade forces

that occur during one revolution. The actuator cylinder concept does no longer include the effect of finite number of blades.

VAWT Modeling Techniques

The previous section presented the blade element model for the VAWT to calculate the performance. However, the blade element model requires an estimation of the inflow at the blade element. In this section, several models for determining the induction field, and therefore the inflow will be presented. Depending on which rotor simplification is considered for further analysis, different modeling techniques are available. The models can be grouped in four main approaches, differing in accuracy and required resources: 1D-based streamtube momentum models, linearized momentum models in the form of the actuator cylinder model, potential flow vorticity-velocity Lagrangian models (usually called *vortex model*), and Eulerian CFD models. While the vortex method and Eulerian CFD method are applicable to all aerodynamic problems, this section will only focus on the VAWT-specific methods. It is not the purpose to compare the models internally. Therefore the reader is referred to Ferreira et al. (2014) for 2D model comparison and to De Tavernier et al. (2020a) and De Tavernier (2021) for 3D comparisons.

1D-Based Streamtube Momentum Models

The 1D momentum theory, used in the development of the actuator disk theory for HAWTs, is a theory describing a mathematical model of a streamtube loaded by a force distribution aligned with the unperturbed flow field, concentrated at a single axial location. The rotor is modeled as an infinitely thin disc with a uniform induced velocity across the streamtube cross-section. The momentum models for VAWTs come in four versions of approximation of the 2D actuator: the single-streamtube model, the multiple streamtube model, the double-streamtube model, and the double-multiple-streamtube model (see Fig. 6).

Templin (1974) was the first to apply the momentum theory to VAWTs, creating the *single-streamtube model*. Templin suggested to evaluate the entire vertical-axis rotor in one streamtube. The complete rotor is replaced by one equivalent actuator disk with a similar thrust coefficient. A consequence of the simplicity of the model is that a single value of induction is determined, and applied over the entire rotor.

Building upon the assumption of streamtube independence used in horizontal-axis rotors, Wilson and Lissaman (1974) and later Strickland (1975) proposed to consider a series of adjacent and independent streamtubes. The sections of the rotor in each streamtube are replaced by one equivalent actuator disk with a loading corresponding to the load present in that streamtube. This method is called the *multiple-streamtube model*. This allows for a cross-flow variation in induction, but still assumed the same induction in the upstream and downstream regions of the actuator.

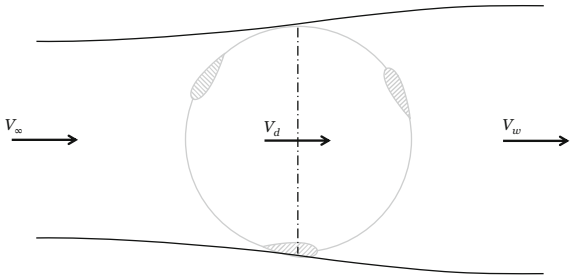

(a) Single-streamtube model

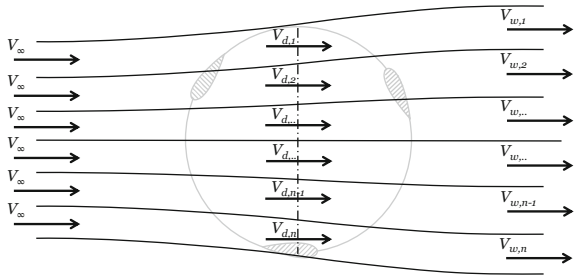

(b) Multiple-streamtube model

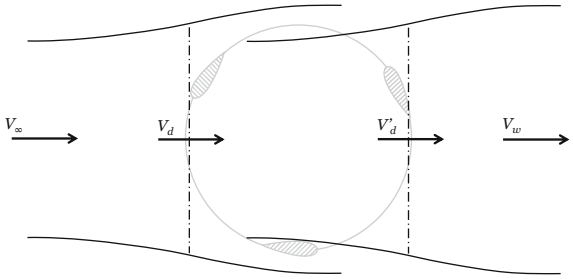

(c) Double-streamtube model

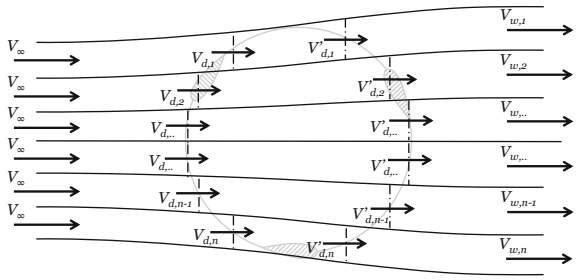

(d) Double-multiple-streamtube model

Fig. 6 Momentum models. (**a**) Single-streamtube model. (**b**) Multiple-streamtube model. (**c**) Double-streamtube model. (**d**) Double-multiple-streamtube model. (Adapted from De Tavernier 2021)

Because the actuator surface crosses the streamtube twice, upwind and downwind, it is relevant to different the value of induction in both regions. In the *double-streamtube model*, the actuator surface is replaced by two actuator disks in series: one for the upwind part and one for the downwind part, with an equivalent thrust. The outlet velocity of the first streamtube is assumed to be the input velocity of the second streamtube, which operates in the developed wake of the first. This slightly more advanced model calculates an induction that is different for the upwind and downwind part of the rotor.

The combination of the double-streamtube model and the multiple-streamtube model was developed by Paraschivoiu (1988), who introduced the so-called *double-multiple-streamtube model*. In this model a series of adjacent aerodynamically independent streamtubes are used in which the upwind and downwind part of the rotor are replaced by different actuator disks with an equivalent loading. This allows the model to determine a different induction for each streamtube and for the upwind and downwind part separately.

As in the actuator disk model for HAWTs, the solution is achieved in an iterative way where the induction from the momentum model is used as input for the blade element model, and the load from the blade element model is introduced in the momentum model. Because the double-multiple-streamtube model is the most complex version using the momentum theory, the equations of this model will be repeated as a tutorial for the four methods (Paraschivoiu 2002). Consider one particular streamtube, as shown in Fig. 7.

The velocity at the upwind actuator section, V_d, is equal to the average of the free-stream velocity V_∞ and the exit velocity V_e. The induction at the upwind actuator section is defined as $a = 1 - V_d/V_\infty$ and $V_e = (1 - 2a)V_\infty$. If it is assumed that the wake of the upwind half is fully developed before reaching the downwind half. The velocity at the downwind actuator section V_d' is the average of V_e and the velocity in the wake V_w. The induction at the downwind actuator section is defined as $a' = 1 - V_d'/V_e$. These relations are expressed in Equations 12 and 13.

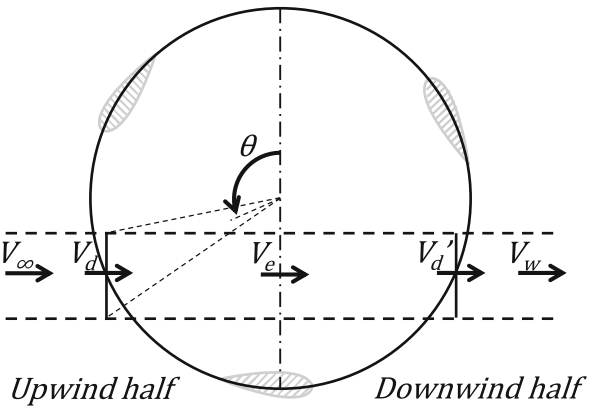

Fig. 7 An isolated streamtube of the double-multiple-streamtube model. (Adapted from De Tavernier 2021)

$$V_d = \frac{V_\infty + V_e}{2} \tag{12}$$
$$= (1-a)V_\infty$$
$$V'_d = \frac{V_e + V_w}{2} \tag{13}$$
$$= (1-a')(1-2a)V_\infty$$

From the blade element theory, the average thrust coefficient at each actuator section in the streamtube can be defined as the time-averaged thrust force T_{avg} divided by $0.5\rho V_\infty^2 A_{st}$, as given by Equation 14. The time-averaged thrust force T_{avg} is basically the instantaneous thrust force T_{inst} at that azimuthal location times how often a blade is passing through that streamtube in one revolution. The instantaneous thrust force is easily defined by blade-element characteristics. A_{st} is the swept area of the streamtube with a height ΔH. $\Delta\theta$ is the width of the streamtube expressed in terms of azimuth angle.

$$C_{T,BEM} = \frac{T_{\text{avg}}}{\frac{1}{2}\rho V_\infty^2 A_{st}} \tag{14}$$

and:

$$T_{\text{avg}} = B\frac{\Delta\theta}{2\pi}T_{\text{inst}}$$
$$T_{\text{inst}} = \frac{1}{2}\rho V_{\text{rel}}^2 c(-C_t\cos(\theta) + C_n\sin(\theta))$$
$$A_{st} = R\Delta\theta\sin(\theta)\Delta H$$

The momentum theory provides a relation between the induction and the loading of the streamtube: $C_T = 4a(1-a)$. By combining this momentum expression with the blade-element equation, a set of equations can be defined for the upwind and the downwind actuator surfaces. These set of equations (Equations 15 and 16) can be solved to obtain a and a' for each streamtube.

Upwind:

$$\begin{cases} C_{T,MOM} = 4a(1-a) \\ C_{T,BEM} = \frac{Bc}{R}\frac{1}{2\pi}\left(\frac{V_{rel}}{V_\infty}\right)^2\left(-C_t\frac{\cos(\theta)}{\sin(\theta)} + C_n\right) \\ C_{T,MOM} = C_{T,BEM} \end{cases} \tag{15}$$

Downwind:

$$\begin{cases} C'_{T,MOM} = 4a'(1-a') \\ C'_{T,BEM} = \frac{Bc}{R}\frac{1}{2\pi}\left(\frac{V'_{rel}}{V_e}\right)^2\left(-C_t\frac{\cos(\theta)}{\sin(\theta)}+C_n\right) \\ C'_{T,MOM} = C'_{T,BEM} \end{cases} \tag{16}$$

To set up the equations of the momentum models, some assumptions are made. Firstly, it is assumed that the wake of the upwind half is fully developed before reaching the downwind half. As such it is assumed that atmospheric pressure is reached in the center of the turbine. Also, the original double-multiple-streamtube model that is proposed by Paraschivoiu (1988) uses straight streamtubes while it is known that the streamtube expands. Read and Sharpe (1980) have proposed a method to include flow expansion. A third assumption is that the streamtubes are assumed to be strictly independent. This means that the loads present in one streamtube do not have any influence on any other streamtube. Finally, the double-multiple-streamtube model neglects the effect of the downwind actuator disk on the upwind disk. Although simple and useful, momentum-based models rely on assumptions that significantly contradict the force field and flow field of the VAWT.

Besides the overall limitations of the streamtube models, several researchers proposed additions to capture more physics with the streamtube momentum models. One of these additions is the inclusion of struts. A strut model has been implemented by Moran (1977), who derived a correction coefficient for the drag. Inclined struts will also produce torque and therefore Goude (2012) and later Hara et al. (2014) proposed a more general approach to include both lift and drag forces. They developed models with the purpose to extend the original multiple-streamtube model to simulate a 2D double-bladed VAWT. An extended version of the double-multiple-streamtube model, namely the improved double-multiple-streamtube (IDMS) approach, has been introduced by Bangga et al. (2019, 2020a). This approach revised the formulation for the flow curvature and wake expansion effects. Finally, the unsteady blade element momentum method (UBEM) should be noted here. The model is inspired from unsteady blade element momentum methods (UBEM) for HAWTs (in the time domain) and is introduced by Hansen in Bangga et al. (2020a) and Hansen (2008). Here the axial induction is determined from the momentum equation by balancing the momentum loss over the rotor with the thrust force, while applying a time filter.

2D Actuator Cylinder Model

The 2D actuator cylinder model was developed by Madsen (1983). It uses a 2D formulation of the momentum equations that favors the application of a linearized form of the equations. The actuator cylinder model requires the external force field as input. For this, an iterative approach with a blade element model is often used: (1) use the blade element model to determine the force field from the velocity field

outputted from the actuator cylinder model; (2) use the actuator cylinder model to the flow field by using the a force field outputted from the blade element model.

Following the procedure in Madsen (1982), the derivation of the actuator cylinder model starts by applying the average reaction of the blade forces as distributed body forces on the flow: a non-dimensional time-averaged normal and a tangential loading (per unit span). The normal and tangential aerodynamic forces are multiplied by the number of blades $B/2\pi$ that will serve as time-averaging in one revolution. They are non-dimensionalized with ρV_∞^2. Non-dimensionalizing with ρV_∞^2 will be a smart choice for the continuation of the derivation. The non-dimensional loading components are recalled as Q_n and Q_t in the normal and tangential direction, respectively (Fig. 8).

$$Q_n(\theta) = \frac{B F_n(\theta)}{2\pi R \rho V_\infty^2} \tag{17}$$

$$Q_t(\theta) = -\frac{B F_t(\theta)}{2\pi R \rho V_\infty^2} \tag{18}$$

Assume that the velocity components are V_x and V_y where u_x and u_y are perturbation terms.

$$\begin{aligned} V_x &= (1 + u_x) V_\infty \\ V_y &= u_y V_\infty \end{aligned} \tag{19}$$

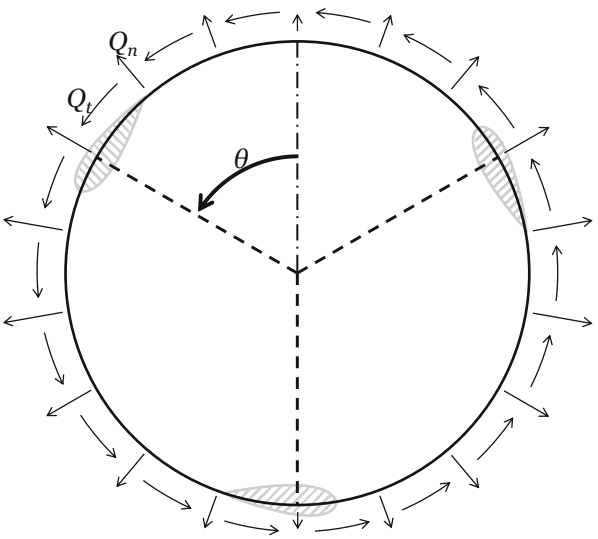

Fig. 8 Actuator cylinder model. (Adapted from De Tavernier 2021)

With this, the 2D steady, incompressible Euler momentum equation as well as the continuity equation can be set up. The Euler momentum equation is basically a set of equations that represent conservation of mass (continuity), and balance the momentum and the energy. The incompressible Euler equations in case of constant density say that the substantial derivative of the flow velocity vector is equal to the gradient of the pressure normalized with the density plus the volume forces per unit mass. The equations, as shown in Equations 20 and 21, are in its convective form. p is the pressure and f are the volume forces.

$$\frac{D\overrightarrow{V}}{Dt} = -\nabla\left(\frac{\overrightarrow{p}}{\rho_0}\right) + \frac{\overrightarrow{f}}{\rho} \tag{20}$$

$$\nabla \cdot \overrightarrow{V} = 0 \tag{21}$$

By substituting the velocity components of Equation 19 into the Euler and continuity equation, Equations 22, 23, and 24 are obtained. The Euler equation is split up in the x- and y-direction. The last two terms of the Euler momentum equations are second-order terms. These terms can be seen as the induced or second-order forces g_x.

$$\frac{du_x}{dx} = -\frac{dp}{dx}\frac{1}{\rho V_\infty^2} + f_x\frac{1}{\rho V_\infty^2} - u_x\frac{du_x}{dx} - u_y\frac{du_x}{dy} \tag{22}$$

$$\frac{du_y}{dx} = -\frac{dp}{dy}\frac{1}{\rho V_\infty^2} + f_y\frac{1}{\rho V_\infty^2} - u_x\frac{du_y}{dx} - u_y\frac{du_y}{dy} \tag{23}$$

$$\frac{du_x}{dx} + \frac{du_y}{dy} = 0 \tag{24}$$

Equations 22, 23, and 24 can be combined into one equation. Differentiate the first Euler equation with respect to x, the second Euler equation with respect to y and the continuity equation with respect to x. Consequently, substitute the differentiated Euler equations into the differentiated continuity equation. This results in Equation 25.

$$\frac{d^2p}{dx^2} + \frac{d^2p}{dy^2} = \left(\frac{df_x}{dx} + \frac{df_y}{dy}\right) + \left(\frac{dg_x}{dx} + \frac{dg_y}{dy}\right) \tag{25}$$

Equation 25 is a Poisson type equation ($\nabla^2 q = \overrightarrow{\nabla}\left(\overrightarrow{f} + \overrightarrow{g}\right)$) that can be simplified to the Laplace equation since the force field f only applies on the actuation surface and the non-linear terms g_x and g_y can be ignored if we are looking for the linear solution. The solution is given by Green's function in which the source term is transformed into a doublet term. As such, the linear solution of the pressure field is given by Equation 26 and the linear solution of the velocity terms u and v are given by Equations 27 and 28.

$$p(f) = \frac{1}{2\pi} \int_S \frac{f_x(x-\eta)}{(x-\eta)^2 + (y-\zeta)^2} + \frac{f_y(y-\zeta)}{(x-\eta)^2 + (y-\zeta)^2} d\eta d\zeta \tag{26}$$

and:

$$u_x(f) = -p(f)\frac{1}{\rho V_\infty^2} + \frac{1}{\rho V_\infty^2} \int_{-\infty}^{x} f_x dx' \tag{27}$$

$$u_y(f) = \frac{1}{\rho V_\infty^2} \int_{-\infty}^{x} \frac{\partial}{\partial y} p(f) dx' + \frac{1}{\rho V_\infty^2} \int_{-\infty}^{x} f_y dx' \tag{28}$$

For an actuator cylinder with the normal and tangential loading Q_n and Q_t, the linear equations for u_x and u_y can be written out as Equations 29 and 30, respectively. Q_n and Q_t are known parameters from the blade element theory. The fractions in these equations are simply depending on the geometry. θ is the azimuth angle and x and y are the coordinates of the location at which to determine the induction. This could be either at the rotor or at any location in the velocity field. x and y are normalized with the rotor radius R.

$$\begin{aligned} u_x(x,y) = {} & \frac{1}{2\pi} \int_0^{2\pi} Q_n(\theta) \frac{(x+\sin(\theta))\sin(\theta) - (y-\cos(\theta))\cos(\theta)}{(x+\sin(\theta))^2 + (y-\cos(\theta))^2} d\theta \\ & + \frac{1}{2\pi} \int_0^{2\pi} Q_t(\theta) \frac{(x+\sin(\theta))\cos(\theta) + (y-\cos(\theta))\sin(\theta)}{(o+\sin(\theta))^2 + (y-\cos(\theta))^2} d\theta \\ & - Q_n(\cos^{-1}(y)) - Q_t(\cos^{-1}(y)) \frac{y}{\sqrt{1-y^2}} \quad \text{(in the cylinder and wake)} \\ & + Q_n(-\cos^{-1}(y)) - Q_t(-\cos^{-1}(y)) \frac{y}{\sqrt{1-y^2}} \quad \text{(in the wake)} \end{aligned} \tag{29}$$

$$\begin{aligned} u_y(x,y) = {} & \frac{1}{2\pi} \int_0^{2\pi} Q_n(\theta) \frac{(x+\sin(\theta))\cos(\theta) + (y-\cos(\theta))\sin(\theta)}{(x+\sin(\theta))^2 + (y-\cos(\theta))^2} d\theta \\ & - \frac{1}{2\pi} \int_0^{2\pi} Q_t(\theta) \frac{(x+\sin(\theta))\sin(\theta) - (y-\cos(\theta))\cos(\theta)}{(x+\sin(\theta))^2 + (y-\cos(\theta))^2} d\theta \end{aligned} \tag{30}$$

Note that there are two terms in the u_x-equation that are only added if your evaluation point is in the wake of the rotor or inside the rotor. These terms originate from the fact that there are infinite solutions to an integral that differ with a constant value. To obtain a continuous velocity field when crossing the rotor, these extra terms should be introduced.

The solution given by Equations 29 and 30 contain only the linear part of the solution. To avoid solving the computationally expensive nonlinear part of the solution, a modified-linear solution is proposed (Madsen et al. 2013). A correction term k_a is introduced to compensate for the non-linear part. This term depends on the thrust coefficient and is used to amplify the linear induction. a is the equivalent induction factor for the total thrust coefficient on the rotor using actuator disk theory.

$$(u_x, u_y) = k_a \cdot (u_x, u_y)_{\text{linear}} \tag{31}$$

and:

$$\text{for } a <= 0.15: \qquad k_a = \frac{1}{1-a}$$

$$\text{for } a >= 0.15: \qquad k_a = \frac{1}{1-a} \cdot \left[0.65 + 0.35\exp(-4.5(a-0.15))\right] \tag{32}$$

Theoretically, the actuator cylinder model is expected to be more accurate than the momentum models. This is true because the actuator cylinder model does take into account the effect from one element or streamtube on the other and also the effect from the downwind part of the actuator on the upwind part of the actuator. This was not the case in the momentum models. More details of the derivation can be found in Madsen (1982, 1983, 1985).

For the actuator cylinder model, also various additions/corrections have been proposed. Researchers such as Ning (2016) and Li (2017) extended the actuator cylinder theory for multiple VAWTs next to each other. De Tavernier and Ferreira (2019) used the actuator cylinder theory to model two concentric actuator cylinders as a way to, for example, represent double-bladed VAWTs or cope with (torque-producing) struts. Although that the 3D actuator cylinder model can be derived in a rather similar way (see section "3D Actuator Cylinder Model"), a 3D rotor is sometimes approached by stacking 2D independent slices. In HAWC2 (Madsen et al. 2013), this stacking approach is used while a correction is implemented based on a near wake model for trailing vorticity to include tip loss effect. The original method is developed by Beddoes (1987) but recently modified by Pirrung et al. (2016, 2017a). The VAWT version of the model is based on the straight wake extension presented in Pirrung et al. (2017b).

3D Actuator Cylinder Model

The 3D actuator cylinder model is a less known method for the modeling of the VAWT. It shares the same derivation as the 2D actuator cylinder model, but with an additional dimension. Because the derivation is not easily available, in this section the 3D linearized momentum equations are derived, as has been done in the previous section for the 2D case.

The 3D actuator cylinder model is a 3D formulation of the momentum equations that favors the application of a linearized form of the equations. The formulation used in this work is adapted from the derivation presented by von Kármán and Burgers in Chapter III, Section 6 of the book *Aerodynamic Theory* edited by Durand (1935).

Assuming that the flow is 3D, and that the main flow direction is in the x-direction, the velocity $\vec{V}$ can be defined in Cartesian coordinates by perturbations in relation to the unperturbed flow as

$$V_x = (1 + u_x)V_\infty \tag{33}$$
$$V_y = u_y V_\infty$$
$$V_z = u_z V_\infty$$

As V_∞ is constant, the 3D momentum and continuity equations can therefore be simplified as:

$$\frac{\partial u_x}{\partial x} + u_x\frac{\partial u_x}{\partial x} + u_y\frac{\partial u_x}{\partial y} + u_z\frac{\partial u_x}{\partial z} = -\frac{\partial p}{\partial x}\frac{1}{\rho V_\infty^2} + f_x\frac{1}{\rho V_\infty^2} \tag{34}$$

$$\frac{\partial u_y}{\partial x} + u_x\frac{\partial u_y}{\partial x} + u_y\frac{\partial u_y}{\partial y} + u_z\frac{\partial u_y}{\partial z} = -\frac{\partial p}{\partial y}\frac{1}{\rho V_\infty^2} + f_y\frac{1}{\rho V_\infty^2} \tag{35}$$

$$\frac{\partial u_z}{\partial x} + u_x\frac{\partial u_z}{\partial x} + u_y\frac{\partial u_z}{\partial y} + u_z\frac{\partial u_z}{\partial z} = -\frac{\partial p}{\partial z}\frac{1}{\rho V_\infty^2} + f_z\frac{1}{\rho V_\infty^2} \tag{36}$$

$$\frac{\partial u_x}{\partial x} + \frac{\partial u_y}{\partial y} + \frac{\partial u_z}{\partial z} = 0 \tag{37}$$

By rearranging the second degree terms, for example in the x-direction, Equation 38 is obtained where $\omega_{x,y,z}$ is the vorticity in the x, y, or z direction, respectively.

$$u_x\frac{\partial u_x}{\partial x} + u_y\frac{\partial u_x}{\partial y} + u_z\frac{\partial u_x}{\partial z} = \frac{\partial}{\partial x}\left(\frac{u_x^2 + u_y^2 + u_z^2}{2}\right) + \frac{\omega_y u_z}{V_\infty^2} - \frac{\omega_z u_y}{V_\infty^2} \tag{38}$$

The momentum equations can be rewritten by moving all the terms that are of second degree in the perturbation quantities to the right side. This results in Equations 39, 40, 41 and is comparable to Equations 22 and 23 as was derived in 2D.

$$\frac{\partial u_x}{\partial x} = -\frac{\partial p}{\partial x}\frac{1}{\rho V_\infty^2} - \frac{\partial}{\partial x}\left(\frac{u_x^2 + u_y^2 + u_z^2}{2}\right) + f_x\frac{1}{\rho V_\infty^2} - \frac{\omega_y u_z}{V_\infty^2} + \frac{\omega_z u_y}{V_\infty^2} \tag{39}$$

$$\frac{\partial u_y}{\partial x} = -\frac{\partial p}{\partial y}\frac{1}{\rho V_\infty^2} - \frac{\partial}{\partial y}\left(\frac{u_x^2 + u_y^2 + u_z^2}{2}\right) + f_y\frac{1}{\rho V_\infty^2} - \frac{\omega_z u_x}{V_\infty^2} + \frac{\omega_x u_z}{V_\infty^2} \tag{40}$$

$$\frac{\partial u_z}{\partial x} = -\frac{\partial p}{\partial z}\frac{1}{\rho V_\infty^2} - \frac{\partial}{\partial z}\left(\frac{u_x^2 + u_y^2 + u_z^2}{2}\right) + f_z\frac{1}{\rho V_\infty^2} - \frac{\omega_x u_y}{V_\infty^2} + \frac{\omega_y u_x}{V_\infty^2} \tag{41}$$

We now define a quantity q as:

$$q = p + \rho\frac{u_x^2 + u_y^2 + u_z^2}{2}V_\infty^2 - p_0 \tag{42}$$

where p_0 is the unperturbed pressure at infinity, which is constant.

By introducing this quantity q in Equations 39, 40, and 41, the equations can be rewritten in the form:

$$\frac{\partial u}{\partial x} = -\frac{\partial q}{\partial x}\frac{1}{\rho V_\infty^2} + f_x\frac{1}{\rho V_\infty^2} + g_x\frac{1}{\rho V_\infty^2} \tag{43}$$

$$\frac{\partial v}{\partial x} = -\frac{\partial q}{\partial y}\frac{1}{\rho V_\infty^2} + f_y\frac{1}{\rho V_\infty^2} + g_y\frac{1}{\rho V_\infty^2} \tag{44}$$

$$\frac{\partial w}{\partial x} = -\frac{\partial q}{\partial z}\frac{1}{\rho V_\infty^2} + f_z\frac{1}{\rho V_\infty^2} + g_z\frac{1}{\rho V_\infty^2} \tag{45}$$

where:

$$g_x = \rho\left(u_y\omega_z - u_z\omega_y\right) \tag{46}$$

$$g_y = \rho\left(u_z\omega_x - u_x\omega_z\right) \tag{47}$$

$$g_z = \rho\left(u_x\omega_y - u_y\omega_x\right) \tag{48}$$

The system of equations, Equations 43, 44, and 45, is an exact representation of fluid motion. On the other hand, if we neglect the nonlinear terms $g_{x,y,z}$, the solution is a first approximation of flow field. The terms of vorticity $g_{x,y,z}$ are then treated as a force term, sometimes named as *induced forces*. For actuator disks with significant loading, the $g_{x,y,z}$ terms are significant. The solution where $g_{x,y,z}$ are neglected is referred to as the *linear solution*. An iterative approach can be used to achieve the full solution, while starting from the linear solution. This is addressed in Durand (1935). However, here we will focus on the linear solution only. Engineering corrections can be applied to correct for the nonlinear part of the solution, as has been discussed in the 2D actuator cylinder model.

By taking the divergence of the system of equations, given in Equations 43, 44, and 45, and summing the three equations, Equation 49 will be obtained.

$$\frac{\partial^2 q}{\partial x^2} + \frac{\partial^2 q}{\partial y^2} + \frac{\partial^2 q}{\partial z^2} = \left(\frac{\partial f_x}{\partial x} + \frac{\partial f_y}{\partial y} + \frac{\partial f_z}{\partial z}\right) + \left(\frac{\partial g_x}{\partial x} + \frac{\partial g_y}{\partial y} + \frac{\partial g_z}{\partial z}\right) \tag{49}$$

This equation has the form of a Poisson type equation ($\nabla^2 q = \vec{\nabla}\left(\vec{f} + \vec{g}\right)$). As q tend to zero at infinity, the Poisson type equation can be solved using Green's function. The solution for the field q is then given by Equation 50 where the integration coordinate system η, ζ, and χ overlaps with the x,y,z coordinate system, and $\vec{f}$ and $\vec{g}$ are a set as functions with respect to η, ζ, and χ. To simplify the equation, a force field $\vec{k} = \vec{f} + \vec{g}$ can be introduced, and thus Equation 50 becomes Equation 51.

$$q_{(f,g,x,y,z)} = \frac{1}{4\pi}\iiint \frac{f_x\,(x-\eta)+f_y\,(y-\zeta)+f_z\,(z-\chi)}{\left((x-\eta)^2+(y-\zeta)^2+(z-\chi)^2\right)^{\frac{3}{2}}}d\eta d\zeta d\chi + \frac{1}{4\pi}\iiint \frac{g_x\,(x-\eta)+g_y\,(y-\zeta)+g_z\,(z-\chi)}{\left((x-\eta)^2+(y-\zeta)^2+(z-\chi)^2\right)^{\frac{3}{2}}}d\eta d\zeta d\chi \tag{50}$$

$$= \frac{1}{4\pi}\iiint \frac{k_x\,(x-\eta)+k_y\,(y-\zeta)+k_z\,(z-\chi)}{\left((x-\eta)^2+(y-\zeta)^2+(z-\chi)^2\right)^{\frac{3}{2}}}d\eta d\zeta d\chi \tag{51}$$

This solution for q in Equation 51 can be combined with the system of equations presented in Equations 43, 44, and 45. But first, the existence of a function Φ and a set of perturbation terms $u'_{x,y,z}$ is introduced, such that the velocity perturbation terms are given by Equations 52, 53, and 54.

$$u_x = u'_x + \frac{\partial \Phi}{\partial x} \tag{52}$$

$$u_y = u'_y + \frac{\partial \Phi}{\partial y} \tag{53}$$

$$u_z = u'_z + \frac{\partial \Phi}{\partial z} \tag{54}$$

$\partial u'_{x,y,z}/\partial x$ is given by Equations 55, 56, and 57

$$\frac{\partial u'_x}{\partial x} = \frac{k_x}{V_\infty^2 \rho} \tag{55}$$

$$\frac{\partial u'_y}{\partial x} = \frac{k_y}{V_\infty^2 \rho} \tag{56}$$

$$\frac{\partial u'_z}{\partial x} = \frac{k_z}{V_\infty^2 \rho} \tag{57}$$

and thus $u'_{x,y,z}$ can be solved by integrating $\partial u'_{x,y,z}/\partial x$ along x. Infinitely upstream ($x = -\infty$), with respect to where the forces are applying, we have no perturbations and thus the boundary condition becomes: $\left[u_x, u_y, u_x\right]_{x=-\infty} = [0, 0, 0]$. Therefore, $u'_{x,y,z}$ is given by Equations 58, 59, and 60, where η is the integration variable.

$$u'_x = \frac{1}{V_\infty^2 \rho}\int_{-\infty}^{x} k_x d\eta \tag{58}$$

$$u'_y = \frac{1}{V_\infty^2 \rho}\int_{-\infty}^{x} k_y d\eta \tag{59}$$

$$u'_z = \frac{1}{V_\infty^2 \rho}\int_{-\infty}^{x} k_z d\eta \tag{60}$$

Combining the sets of equations, given by Equations 52, 53, and 54 and Equations 58, 59, and 60, in combination with the system of equations from Equations 43, 44, and 45 implies that Equation 61 is true.

$$\frac{\partial \Phi}{\partial x} = -\frac{q}{\rho V_\infty^2} \tag{61}$$

By substituting Equation 51 in Equation 61 and integrating along ξ from $x = -\infty$ to x, we can now obtain $\Phi_{(x,y,z)}$. The integration variable ξ is parallel to x and η. At $x = -\infty$, $q = 0$, which means that $\Phi_{x=-\infty}$ =constant. The integral can be written as Equation 63 where $r = \sqrt{(x-\eta)^2 + (y-\zeta)^2 + (z-\chi)^2}$.

$$\Phi_{(k,x,y,z)} = \int_{-\infty}^{x} \left(-\frac{1}{4\pi\rho V_\infty^2} \iiint \frac{k_x\,(x-\eta) + k_y\,(y-\zeta) + k_z\,(z-\chi)}{\left((x-\eta)^2 + (y-\zeta)^2 + (z-\chi)^2\right)^{\frac{3}{2}}} d\eta d\zeta d\chi \right) d\xi \tag{62}$$

$$= \frac{1}{4\pi\rho V_\infty^2} \iiint \frac{k_x}{r} - \frac{k_y\,(y-\zeta) + k_z\,(z-\chi)}{r\,(r-(x-\eta))} d\eta d\zeta d\chi \tag{63}$$

Finally, by substituting the solutions for $\Phi_{(x,y,z)}$ and $u'_{x,y,z}$ into Equation 52, the resulting expressions for the linear solution of $u_{x,y,z}$ become:

$$u_x = \frac{1}{4\pi V_\infty^2 \rho} \iiint -\frac{k_x\,(x-\eta) + k_y\,(y-\zeta) + k_z\,(z-\chi)}{r^3} d\eta d\zeta d\chi + \frac{1}{V_\infty^2 \rho} \int_{-\infty}^{x} k_x d\eta \tag{64}$$

$$\begin{aligned} u_y = & \frac{1}{4\pi\rho V_\infty^2} \iiint -k_x \frac{(y-\zeta)}{r^3} d\eta d\zeta d\chi + \\ & \frac{1}{4\pi\rho V_\infty^2} \iiint k_y \frac{\left(r^2 - (y-\zeta)^2\right)(r-(x-\eta)) + (y-\zeta)^2 r}{r^3\,(r-(x-\eta))^2} d\eta d\zeta d\chi + \\ & \frac{1}{4\pi\rho V_\infty^2} \iiint k_z \frac{(z-\chi)\,(y-\zeta)\,(2r-(x-\eta))}{r^3\,(r-(x-\eta))^2} d\eta d\zeta d\chi + \\ & \frac{1}{V_\infty^2 \rho} \int_{-\infty}^{x} k_y d\eta \end{aligned} \tag{65}$$

$$u_z = \frac{1}{4\pi\rho V_\infty^2} \iiint -k_x \frac{(z-\chi)}{r^3} d\eta d\zeta d\chi + \frac{1}{4\pi\rho V_\infty^2} \iiint k_z \frac{\left(r^2 - (z-\chi)^2\right)(r-(x-\eta)) + (z-\chi)^2 r}{r^3 (r-(x-\eta))^2} d\eta d\zeta d\chi + \frac{1}{4\pi\rho V_\infty^2} \iiint k_y \frac{(y-\zeta)(z-\chi)(2r-(x-\eta))}{r^3 (r-(x-\eta))^2} d\eta d\zeta d\chi + \frac{1}{V_\infty^2 \rho} \int_{-\infty}^{x} k_z d\eta \tag{66}$$

Unsteady Aerodynamics

Due to the continuous variation of the force field and the inflow perceived by the blades, unsteady effects are of vital importance to be included in the modeling of VAWTs. The bound circulation is changing with the azimuthal position, resulting in a varying wake strength. Therefore phenomena such as dynamic stall, blade-vortex interaction, and flow curvature are of vital importance during VAWT operation.

Dynamic Stall

Although many authors use the term dynamic stall to also address the modeling of attached unsteady aerodynamics, we will focus on the phenomena of unsteady flow separation and stall. The term dynamic stall typically represents the coupling between the trailing edge separation and the leading edge separation in case the airfoil is exposed to a variation in the pressure distribution and boundary layer development, often due to a change in perceived inflow over the airfoil's surface.

There are typically four phases in dynamic stall: (1) trailing edge separation is initiated, (2) a leading edge vortex will be formed, start to grow, and roll up as it convects downstream, (3) the flow will fully separate as the vortex passes the trailing edge, and (4) the flow start to reattach and the aerodynamic loads return to the pre-stalled values. This is summarized in Fig. 9.

With this section, it is not the purpose to address the full topic of dynamic stall. Instead we will focus on the relevance for VAWTs, the vortex dynamics particularly for VAWTs with fixed-pitch blades, and how dynamic stall may be integrated in VAWT modeling techniques.

Relevance for VAWTs

Dynamic stall is a relevant phenomenon for vertical-axis wind turbines both in the design and during operation, as it impacts the turbine loading and the control and wake dynamics. This is particularly true for stall regulated VAWTs, where dynamic stall is common. The movement of the blades in a VAWT entails a variation of

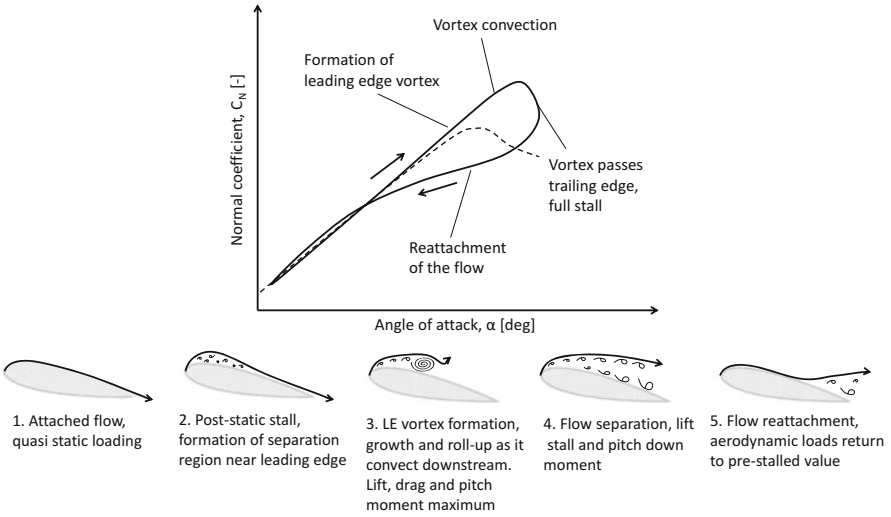

Fig. 9 Phases in dynamic stall. (This figure is reproduced from Dyachuk and Goude (2015) and Carr (1988). Adapted from De Tavernier 2021)

tangential and normal velocity perceived by the blade, resulting in a varying angle of attack and dynamic loads. At low tip-speed ratios ($\lambda < 4$), the angle of attack of the blade exceeds the static stall angle and this will often result in dynamic stall. Additionally, turbulent flow and blade-vortex interaction can originate dynamic stall in the windward, leeward, and the downwind regions of the rotor (the last one depending on the rotor loading and the tip speed ratio). Dynamic stall affects the performance of a VAWT at various levels, as has been enumerated in Zanon et al. (2015):

- Dynamic stall will cause increased blade loads with larger load oscillations. This will effect the fatigue life of the turbine.
- As dynamic stall affects the turbine loading, it will also impact the power output of the turbine.
- Dynamic stall significantly affects the control strategy for VAWTs, especially for stall-controlled turbines.
- Dynamic stall will alter the wake development.
- Dynamic stall may result in an increased noise level due to the shedding of large vortices and the subsequent blade-vortex interaction.

Vortex Dynamics During Dynamic Stall

To improve the understanding of dynamic stall for VAWTs, consider the vortex dynamics in the upwind half of the rotor. Figure 10 shows the evolution of the leading and trailing edge separated vortex for $\lambda = 2$ at 90°, 108°, 133°, and 158°, and the roll-up of the trailing edge vorticity at 90°, 108°, and 133°. The flow is

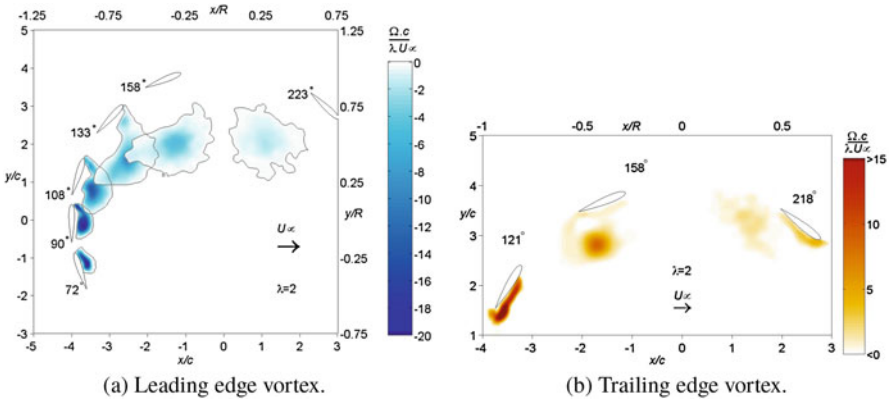

(a) Leading edge vortex. (b) Trailing edge vortex.

Fig. 10 Evolution of the leading and trailing edge separated vortex for $\lambda = 2$ at 90°, 108°, 133°, and 158°, and the roll-up of the trailing edge vorticity at 90°, 108°, and 133°. Ω represents the vorticity of the flow from experimental velocity data. (**a**) Leading edge vortex. (**b**) Trailing edge vortex. (Adapted from Ferreira 2009)

characterized by the shedding of strong vortices. At the leading edge, strong vortices result from leading-edge separation where the clockwise vortices detach from the surface. At the trailing-edge, a wake is formed from the pressure-side boundary layer and the boundary layer develops on the suction side, aft of the reattachment point of the separated leading edge flow. This wake is formed at the trailing edge of the aerofoil by the merging of the two boundary layers and it experiences a roll-up due to the strong vorticity that is present.

From Fig. 10, it can be seen that at $\theta = 90°$, the vorticity shed at the leading edge has rolled up into a large conglomerate of small vortices in a region with a length of one chord. Yet, the wake at the trailing edge has not yet started to roll up nor move over the suction surface. At $\theta = 120°$, the wake shed at the trailing edge has rolled up and the main counterclockwise vorticity is located over the last quarter of the suction side of the airfoil, between the surface and the leading-edge shed vorticity which has started to convect away from the airfoil.

Dynamic stall is highly dependent on the reduced frequency of the perturbation, a scaling between the frequency of perturbation and the kinematic scales of the flow (chord and perceived velocity). Often, the frequency of the unsteadiness is approximated by the rotational frequency, assuming that the main sources of unsteadiness are the variation of angle of attack and the dynamic pressure. However, this assumption, although useful, does not take into account several factors, such as:

- The variation between the points of maximum value of angle of attack, dynamic pressure, and lift for the upwind blade-passage and their corresponding values for the downwind blade-passage occurs as a faster process in the leeward movement

of the blade than in the windward movement of the blade. Therefore, the reduced frequency varies significantly during the rotation.

- The blade-vortex interaction that occurs in the downwind passage and during all the leeward movement of the blade causes the near wake of the blade generated in the upwind passage to be convected with the blade in the leeward movement. The resulting variation of the strength of the shed wake means that the blade-vortex interaction will occur with discrete, strong vortices, resulting in high-frequency oscillations of the forces.
- The shedding of strong, discrete, separated leading-edge vortices, traveling over the upper surface and the trailing edge of the blade, will result in fast oscillations of the pressure field and the force around the blade.
- In the upwind side, the leading edge vortex remains attached longer due to the curved motion as it is on the inside of the rotor, while for the downwind side it detaches earlier due to being on the outside of the rotor.

Modeling Dynamic Stall

Dynamic stall will impact the wake dynamics, the vorticity field and will result in a different induction field. The vorticity at the blade leading edge and trailing edge are released at different azimuthal positions and transported differently by the blade (see Zanon et al. 2015). The convection of the vortical structures with the blade means that the geometry of the wake, in presence of viscous effects, differs from what is obtained with models that rely on time averaging of the loading (streamtube momentum models, actuator cylinder models) or single-wake vortex models. Single-wake models continuously shed vortex blobs for a moving airfoils in a region close to the trailing edge (Zanon et al. 2015). This assumption is acceptable in attached flow conditions, but it is violated in case of flow separation.

And thus, the use of extra engineering models is needed to include dynamic stall in various modeling techniques. Different engineering models exist and may be categorized in resynthesize models (fully based on wind tunnel measurement results) and semiempirical models (combining physical equations with empirical coefficients determined from experimental results). Examples are the Boeing-Vertol Gamma function method by Gross and Harris (1969) and Gormont (1973), the ONERA method (Tran and Petot 1981), and the Leishman-Beddoes method (Leishman and Beddoes 1989). While these are first-order models, there are also several second order models such as the Snel model (Snel 1997), Hopf-Biffurcation model (Truong 1993), IAG model (Bangga et al. 2020b), and Adema-Snel model (Adema et al. 2020). Although there are many more studies available in literature that are dedicated to dynamic stall modeling, industry is still relying mostly on the very basic classical dynamic stall models such as the Leishman-Beddoes model or the Snel models. This is mainly because of the simplicity to tune these models for different airfoils and various flow conditions (Bangga et al. 2020b).

Flow Curvature

The 2D circular motion of an airfoil can be decomposed into a translational motion and a constant pitching motion around a pitching axis, meaning the airfoil rotates over itself. This pitching motion results in varying inflow conditions over the surface of the airfoil. Note here that the pitching axis is the intersection between the airfoil and the radius. The effect of the pitching motion is usually referred to as *flow curvature effects*.

Relevance for VAWTs

In the work of Migliore et al. (1980), Hirsch and Mandal (1985), and Cardona (1984), the effect of the blade pitching is identified as an additional angle of attack or camber. Following the methodology proposed by Migliore et al. (1980), the effect of a pitching movement is set equivalent to converting the geometrical airfoil to a virtual airfoil in a rectilinear flow, as is illustrated in Fig. 11. This transformation introduces an additional camber and thus also an additional incidence angle of which the properties depend on the ratio between the chord and the radius c/R and the tip speed ratio λ. The equivalent camber impacts the boundary layer development and blade design.

The effect of flow curvature can also be understood from the potential theory. When applying a linear potential model, such as the $2D$ panel method, the solution for the circulation on the airfoil is a linear summation of the circulation due to the several perturbations over the surface of the blade (Ferreira 2009), namely those due the wind, perturbations induced by the wake, by other airfoils, and by the motion of the blade (see Equation 67).

$$\Gamma_{\text{airfoil}} = \Gamma_{\text{wind}} + \Gamma_{\text{wake}} + \Gamma_{\text{other-airfoil}} + \Gamma_{\text{displacement}} \tag{67}$$

A derivation of the added circulation due to this constant pitching is found in Strickland et al. (1981), which uses a complex potential flow description of the flat

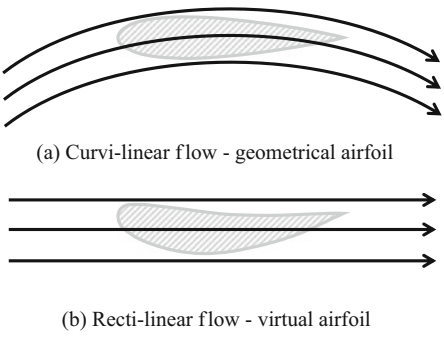

Fig. 11 Interpretation of flow curvature effects as an equivalent transformation of the airfoil, as interpreted by Migliore (1983). (**a**) Curvi-linear flow – geometrical airfoil. (**b**) Recti-linear flow – virtual airfoil. (Adapted from De Tavernier 2021)

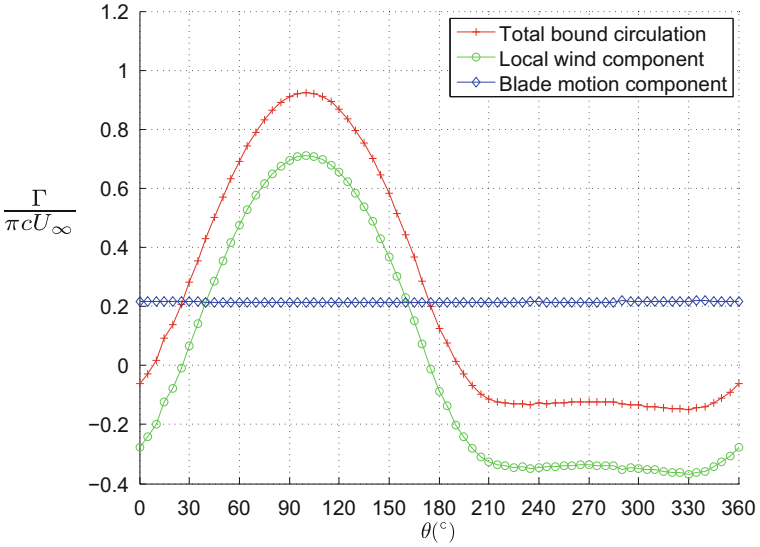

Fig. 12 Bound vorticity for $a_\gamma = \frac{1}{2}$ case; breakdown of total bound circulation into component due to local wind speed and component due to motion of the blade. (Adapted from Ferreira 2009)

plate rotating and translating to determine the different force components, including added-mass effects. A simplified analysis is presented in Equation 68, which defines the circulation of a flat plate as a function of chord c, the (non-dimensionalized) distance from the airfoil midpoint a_γ, the angle of attack α, the perceived wind velocity V, the plunging velocity $\dot{h}$, and the pitching rate $\dot{\gamma}$ (for small angles of attack) (Katz and Plotkin 2001; Leishman 2006).

$$\Gamma = c\pi \left(V \sin(\alpha) + \dot{h} + \frac{c}{2} \left(\frac{1}{2} - a_\gamma \right) \dot{\gamma} \right) \tag{68}$$

The effect of the blade's motion on the bound circulation can be seen in Fig. 12, where the value for total bound circulation is split into the component due to local wind speed and the component due to the steady motion of the blade. The circular motion of the airfoil during the rotation is performed at a constant angular velocity. As such, this contribution remains constant during rotation ($d\Gamma_{\text{displacement}}/dt = 0$). Since the strength of the wake is dependent on the time derivative of the circulation, the displacement of the airfoil (including both translation and pitching movements) has (mostly) no impact on the wake generation in 2D potential flow. This is, however, not true in 3D flow conditions.

Effect of the Pitching Axis

From Equation 68, it is clear that the contribution due to the blade's motion will depend on the pitching rate and the location of the pitching axis. For a fixed pitch

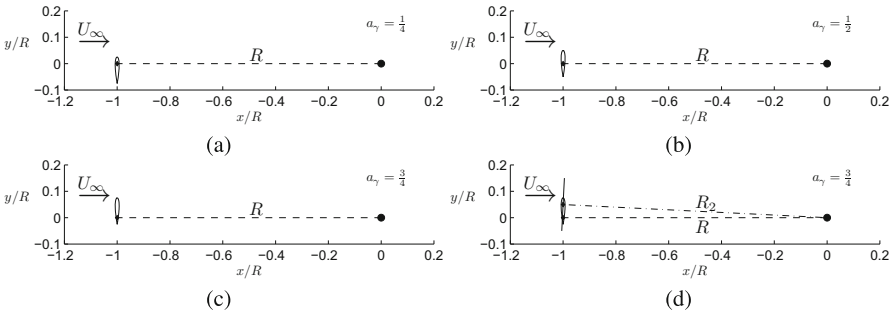

Fig. 13 Schematic of location of the pitching axis of the blade for (**a**) $a_\gamma = \frac{1}{4}$, (**b**) $a_\gamma = \frac{1}{2}$ and $a_\gamma = \frac{3}{4}$. (Adapted from Ferreira 2009)

blade, the pitching rate equals the rotational velocity of the rotor and the location of the pitching axis is a key design variable.

Fig. 13 shows the representation of one of the blades of the rotor, at three different settings for the location of the pitching axis a_γ. From a geometrical point of view, varying the location of the relative position of the pitching axis over the chord is equivalent to changing the rotor radius and introducing a fixed pitch angle, as is illustrated in Fig. 13d. This is consistent with treating the blade as a bound point vortex at the quarter-chord location, where all loading is concentrated. However, in the case of an airfoil, the shape of the surface, and in particular airfoil thickness, will add a second-order effect.

From a $2D$ flow analysis, using a 2D panel model (Ferreira 2009), of a three-bladed rotor with $c/R = 0.1$ at a tip-speed ratio of $\lambda = 4$, the strength of the shed vorticity over the rotation can be determined for various locations of the pitching axis. The distributions of shed vorticity, as indicated in Fig. 12, are almost identical. The discrepancies in the downwind region can be attributed to blade-vortex interaction. The similarity in the distribution of the shed vorticity also implies a similarity in the power coefficient between the three rotors in potential flow (Fig. 14).

However, although the shed vorticity distribution is rather unaffected by the location of the pitching axis, it does impact the instantaneous loading. Fig. 15a shows the tangential force over the rotation for different locations of the pitching axis on the airfoil. The results reveal a transfer of tangential force between the upwind blade passage and the downwind blade passage, or in other words the decrease of torque in the upwind blade passage is compensated by an increase of torque in the downwind blade passage. It is possible to see a decreasing effect of torque ripple with shifting the location of the pitching axis more to the aft region of the chord. Fig. 15b shows the normal force over the rotation for different locations of the pitching axis on the airfoil. Here, a translation of the normal force curve in the normal force direction, can be identified. Note that changing the location of the pitching axis shows a similar behavior when introducing a fixed pitch angle.

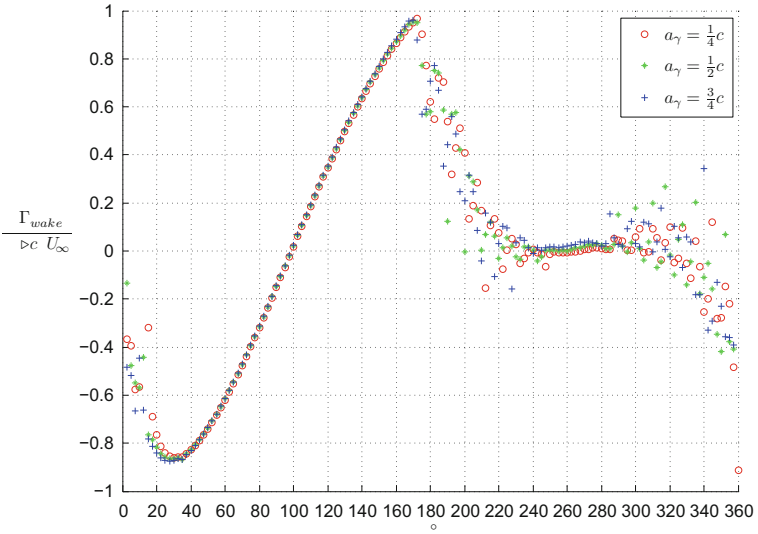

Fig. 14 Shed vorticity for different locations of the pitching axis on the aerofoil. (Adapted from Ferreira 2009)

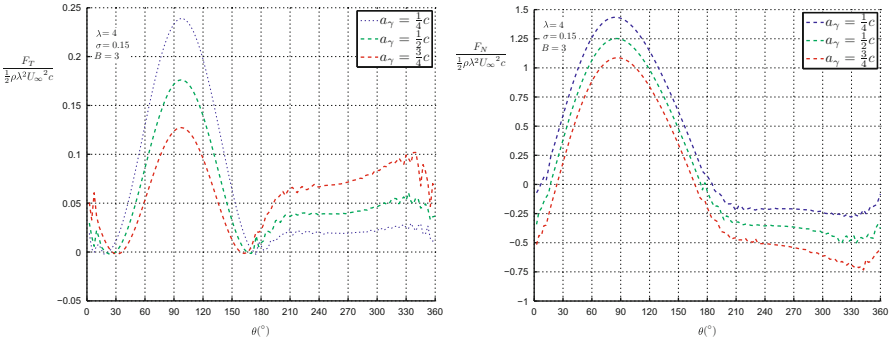

Fig. 15 (**a**) Tangential force and (**b**) normal force for different locations of the pitching axis. (Adapted from Ferreira 2009)

The previously mentioned observations are made for 2D flow. Varying the distribution of bound circulation on the blade does imply a variation of the strength of the trailing vorticity. As such, in $3D$ flow, varying the pitching axis will affect the induction due to trailing vorticity and tip vortex dynamics. The energy conversion process will significantly depend on the aspect ratio of the rotor. 3D effects due to a fixed pitch, as an analogy to shifting the location of the pitching axis, will be handled further in section "Wake Aerodynamics".

Blade-Vortex Interaction

Blade-vortex interaction (BVI) is an inherent feature for VAWTs, a consequence of the orientation of the axis of rotation. Since there is a constant shedding of vorticity from the blades into the wake, the blade passage in the downwind part of the rotor encounters the wake generated in the upwind part (also generated by the other blades). The inflow experienced by the blades during the downwind passage is still dominated by the blade rotation; however, the flow is unsteady and this causes large variation in the induced velocity.

Fig. 16 shows the experimental results of the wake of a VAWT in the region near to the blade (*NACA0015*) at $\theta = 20°$. The experimental plot shows three different wake segments: (1) the new wake released from the trailing edge of the blade (blue-red vorticity curve emanating from trailing edge), (2) the wake segment generated by the other blade, that is now crossed by this blade (yellow vorticity curve crossing blade), (3) the portion of the wake generated by this blade, during the previous revolution (yellow vorticity curve more to the right). The experimental wakes are overlapped with the location of the wake from $2D$ and $3D$ simulations generated by a vortex panel method (Ferreira 2009). The 3D flow field of a VAWT can result in a higher upwind induction than predicted by a 2D model. Such inaccuracy can lead to an incorrect prediction of the location of blade vortex interaction.

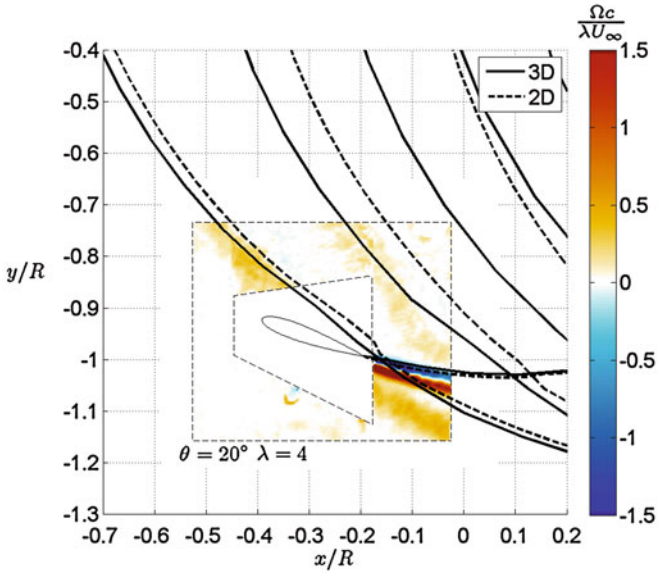

Fig. 16 Blade vortex interaction in the leeward motion of a VAWT blade. Comparison of experimental data (vorticity field) with simulations of the location of the wake as simulated with $2D$ and $3D$ unsteady vortex models ($z/H = 0, \theta = 20°$). (Adapted from Ferreira 2009)

Fig. 17a shows the azimuthal and spanwise distribution of bound circulation on the blade, simulated by a 3D unsteady panel method (Ferreira 2009). The downwind passage bound circulation distribution can be divided into two regions, determined by the sign of bound vorticity. This variation in bound vorticity results from the location of the blade-vortex interaction between the downwind blade passage and the wake generated during the upwind passage. A velocity field, combining the velocity experienced by the blade's rotation with a sign-varying spanwise bound circulation distribution, implies that the normal force distribution also varies in sign along the span. In the tip region, the normal force is in the outward direction, while in the midspan region, the normal force turns inwards (see Fig. 17b). This force distribution has an effect in the bending and fatigue of the blade.

Wake Aerodynamics

The wake of a wind turbine is a direct consequence, and vice versa, of the loading created by the turbine. The thrust force on a rotor will decrease the flow velocity according to the conservation of momentum, which then will cause a flow expansion due to continuity. In this section, the near and far wake of the VAWT will be discussed. Further, different methods on how the wake can be altered for wake deflection purposes will be introduced.

Near and Far Wake

The wake of a vertical-axis wind turbine is significantly different than that of the classical horizontal-axis wind turbine. In this section, the main wake characteristics of a VAWT and the vortex system responsible for this will be introduced. Additionally, a note will be made on the main differences between the wake of a HAWT.

Wake Characteristics

In Fig. 18, the flowfield in the horizontal midplane around a two-bladed turbine at a tip speed ratio of 4.5 is presented. The data is obtained from Tescione et al. (2014) and shows that the lowest flow velocities are expected in the central region. The flow velocity on the sides is slightly higher. Due to momentum conservation, this is consistent with the fact that the thrust force is the largest in the central region where high angles of attack occur.

One can also see the asymmetry of the wake between the leeward and downward region of the flow. Although the flow is already expected to be asymmetric in the cross-flow direction in 2D, the spanwise direction adds an additional effect of asymmetry. The wake roll-up and inboard/outboard movement of the wake will occur differently at the leeward and windward regions. In 2D, the expansion in the windward region of the wake is stronger that in the leeward region. On top of this, also the expansion of the wake in spanwise direction (and the roll-up of the wake close to the tip vortex) is larger in the windward region than in the leeward region.

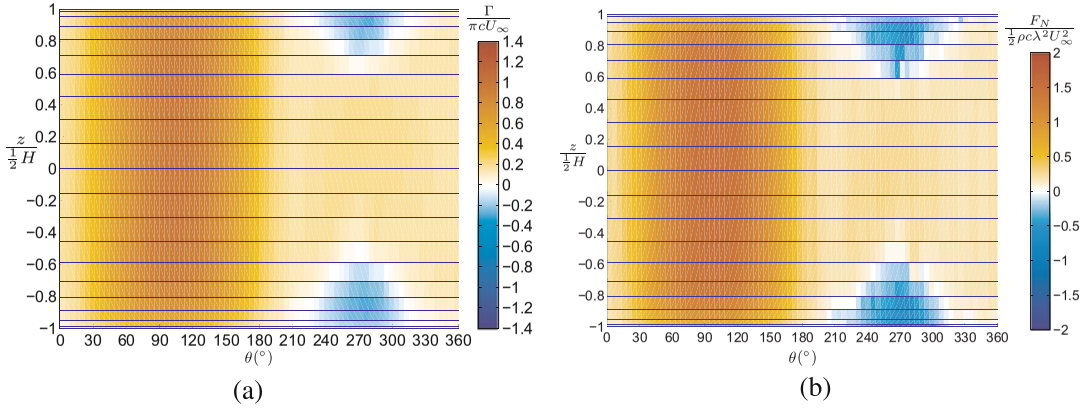

Fig. 17 (**a**) Bound circulation distribution over azimuth and span. (**b**) Spanwise distribution of normal force over the blade during the rotation. (Adapted from Ferreira 2009)

This has the effect that one can expect to see more vertical flow expansion at the windward side, than at the leeward side. The asymmetry is also more prominent at lower tip speed ratios, as the relative difference in relative flow velocity is larger. This is consistent with the available experimental results from Bachant and Wosnik (2015), Rolin and Porté-Agel (2018), and Tescione et al. (2014), where one can see that the experiments with low tip speed ratio have larger asymmetries between both the wake expansion and the corner vortices. As an illustration of the flow generated behind a turbine, the turbine in Tescione et al. (2014) has been simulated using the actuator line model described in Mendoza and Goude (2019) for a uniform flow. Figure 19 shows the velocity deficit (V_x / V_∞) where V_∞ is the inlet velocity of the simulation.

The velocity deficit in the wake of a given turbine will have a significant dependence on the tip speed ratio, where higher tip speed ratios give a higher thrust force and hence a larger decrease in flow velocity. This will also affect the 3D shape of the wake. The measurements in Hara et al. (2011) show that when the tip speed ratio is increased, the vertical contraction at the center of the turbine is amplified. However, in the measurements in Battisti et al. (2011), the increased tip speed ratio does not show any increased contraction in the vertical direction.

In the far-wake region, the structure of the near wake region will change, as the wake will become unstable at some point. Here, a factor that will contribute is the asymmetries of the wake, where one can assume that large asymmetries will trigger instabilities and cause the wake to dissipate earlier. This has given rise to the claim that a VAWT may have a shorter wake than a HAWT (Tescione et al. 2014). In the measurements by Kinzel et al. (2012), the vertical-axis turbine showed a recovery to a velocity deficit of 95% in half the distance (6 turbine diameters) of a typical

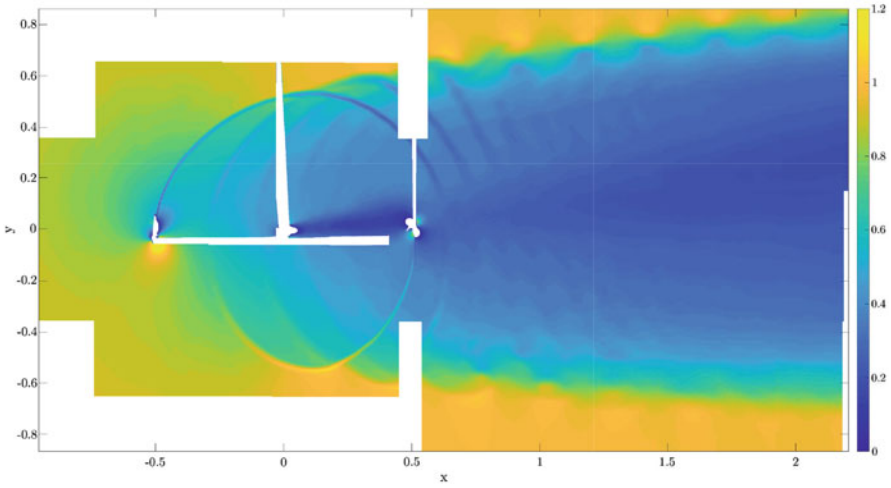

Fig. 18 Normalized velocity (in the x-direction) in the horizontal mid-plane of an experimental VAWT. (Adapted from Tescione et al. 2014)

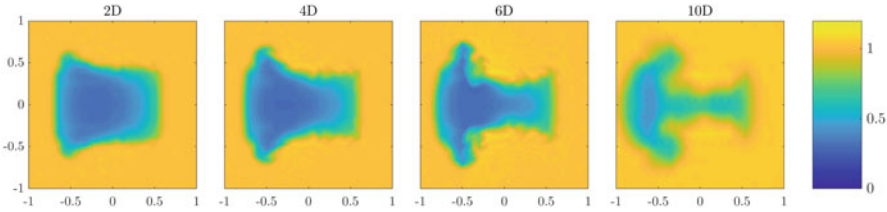

Fig. 19 Simulation of the velocity deficit 2 to 10 diameters behind a turbine using a uniform inflow. The turbine is described in Tescione et al. (2014). The cross-sectional area of the turbine is 1×1 m centered in the figure and ground effects are ignored. (Courtesy of Victor Mendoza)

horizontal-axis turbine. However, one other parameter that needs to be considered is the thrust force.

Wind tunnel measurements often focus on the near-wake region, although there are some studies that extend up to 10 turbine diameters behind the turbine, showing the decay of the wake even better. One of these studies are the measurements of Peng et al. (2016), which show that the maximum velocity deficit is the largest around 2 turbine diameters downstream with values about 75%, while the maximum velocity deficit at 10 turbine diameters is only 25%. Rolin and Porté-Agel (2018) also measured a VAWT up to 10 diameters, here in an atmospheric boundary layer. Also in this study, the largest velocity deficits are measured about 2 turbine diameters behind the turbine (although in this study, 2 diameters is the first measurement position). This study also shows the decay of the corner vortices, where after 6 turbine diameters, only the upper vortex on the leeward side remains, and the wake is pushed sideways similar to Fig. 19. There are several numerical studies that have been performed for the far wake. Shamsoddin and Porté-Agel simulated a vertical-axis wind turbine in an atmospheric boundary layer and found that the maximum velocity deficit occurred at 2.7 turbine diameters and the highest turbulence intensity at 3.8 diameters. A comparison between horizontal-axis and vertical-axis turbines has been performed in Mendoza et al. (2018) with an actuator line model, indicating that the increased thrust force from the vertical-axis turbine will give a slightly larger wake in the far field region, compared to a horizontal-axis turbine of equal size. That study also shows that increased turbulence levels should give faster recovery of the wake. Another study Chatelain et al. (2017) using a vortex method also showed faster wake recovery with increased turbulence levels.

As there are many parameters controlling the wake, such as the aspect ratio (height/diameter), the tip speed ratio (especially if stall occurs which is not covered above), and the thrust force, one should consider that the shape of the wake can vary significantly between different vertical-axis wind turbines, and that the values presented here only serve as representative examples.

Vortex System

To better understand the wake dynamics and the creation of the wake of a VAWT, the vortex system can be considered. The vorticity equation for incompressible, inviscid flows, as given by Equation 69, states that vorticity can only be created by a change in the force field, that is, at the locations where the curl of the forcefield is non-zero. As such, you could say that vorticity is a space-dependent parameter. The created vortex lines consequently move with the flow and convect with the local flow velocity.

$$\frac{D\omega}{Dt} = \underbrace{(\omega \cdot \nabla)u}_{=0,\text{no stretching}} - \underbrace{\omega(\nabla \cdot u)}_{=0,\text{incompressible}} + \underbrace{(\nu\nabla^2\omega)}_{=0,\text{inviscid}} + \nabla \times f = \nabla \times f \tag{69}$$

For simplicity, consider an actuator cylinder (see Fig. 5c) with a prescribed uniform load normal to the surface upwind and a uniform load normal to the surface downwind in the direction against the wind in cylindrical coordinates: radial r, azimuthal θ, and spanwise z-direction. Although these loadings are hypothetical, shaping and shifting the loads may be realized in reality by applying a (variable) blade pitch angle. The curl of the force field simplifies to Equation 70 since the forces are zero except in radial direction.

$$\frac{D\omega}{Dt} = \nabla \times f = \begin{bmatrix} \frac{1}{r}\frac{df_z}{d\theta} - \frac{df_\theta}{dz} \\ -\frac{df_z}{dr} + \frac{df_r}{dz} \\ \frac{df_\theta}{dr} - \frac{1}{r}\frac{df_r}{d\theta} \end{bmatrix} = \begin{bmatrix} 0 \\ \frac{df_r}{dz} \\ -\frac{1}{r}\frac{df_r}{d\theta} \end{bmatrix} \tag{70}$$

In 2D, df_r/dz vanishes out and thus the curl of the forcefield is only non-zero in the z-direction at the poles when going from the upwind to the downwind half of the rotor ($df_r/d\theta \neq 0$). As such vorticity will be created at these points only. The strength of the vortex corresponds to the variation in the load and not to the load itself. As such, it is independent on how the loads are distributed between the upwind and downwind half.

In 3D, df_r/dz will no longer vanish and is non-zero at the top and bottom of the cylinder. This causes an extra creation of vorticity around the azimuthal direction. For a non-uniformly loaded actuator cylinder (both in spanwise or azimuthal direction), also vorticity would be shed at other elements. To clarify this further, a schematic of the vortex system of a uniformly loaded actuator cylinder with hypothetically all loads upwind and all loads downwind (with a fixed convecting velocity) is provided in Fig. 20. The 3D vortex system including vorticity around the azimuthal- and z-direction is no longer the same when redistributing the loads between the upwind and downwind half, although this was true in 2D. The creation of these 3D vortex systems will cause the rotor and wake induction to be different than the 2D case.

From these vortex systems, it may be understood that the presence of tip vortices will cause the vorticity field and thus the velocity field to be significantly different

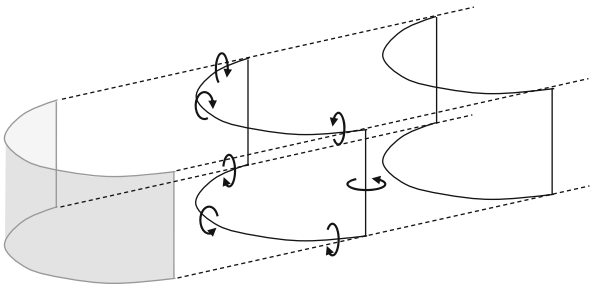

(a) All load upwind

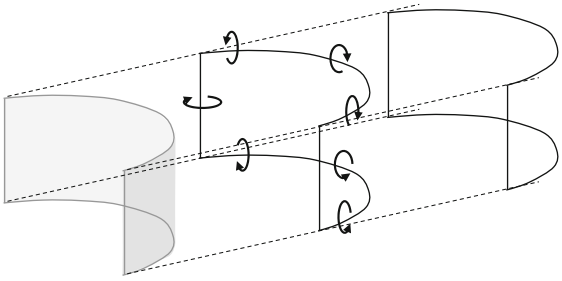

(b) All load downwind

Fig. 20 The vortex system of a uniformly normal loaded actuator cylinder with (**a**) all load upwind and (**b**) all load downwind. (Adapted from De Tavernier et al. 2020b)

when considering various load configurations. In case all the load is located at the upwind part of an actuator cylinder, the trailing vortices deform the wake by pushing the flow from above (and below) inside the wake. In case all load is concentrated downwind, the trailing vortices are pushing the flow from cross-flow direction inside the wake. A clear roll-up is visible when moving further downstream. When the load is distributed between the upwind and downwind part of the rotor, both effects are combined. In Fig. 21, the wake of various load configurations is provided.

Wake Deflection

The idea behind wake deflection is to improve the performance of a wind farm. When a wind turbine operates in the wake of another, the energy extraction is decreased significantly. Hence, there are significant performance gains to be achieved if the wake of the first turbine can be deflected so the second turbine no longer operates in it. Wake deflection techniques are based on generating a force component perpendicular to the wind direction from the turbine, which according to momentum conservation means that the flow is deflected in the opposite direction. There are two approaches suggested for vertical-axis turbines.

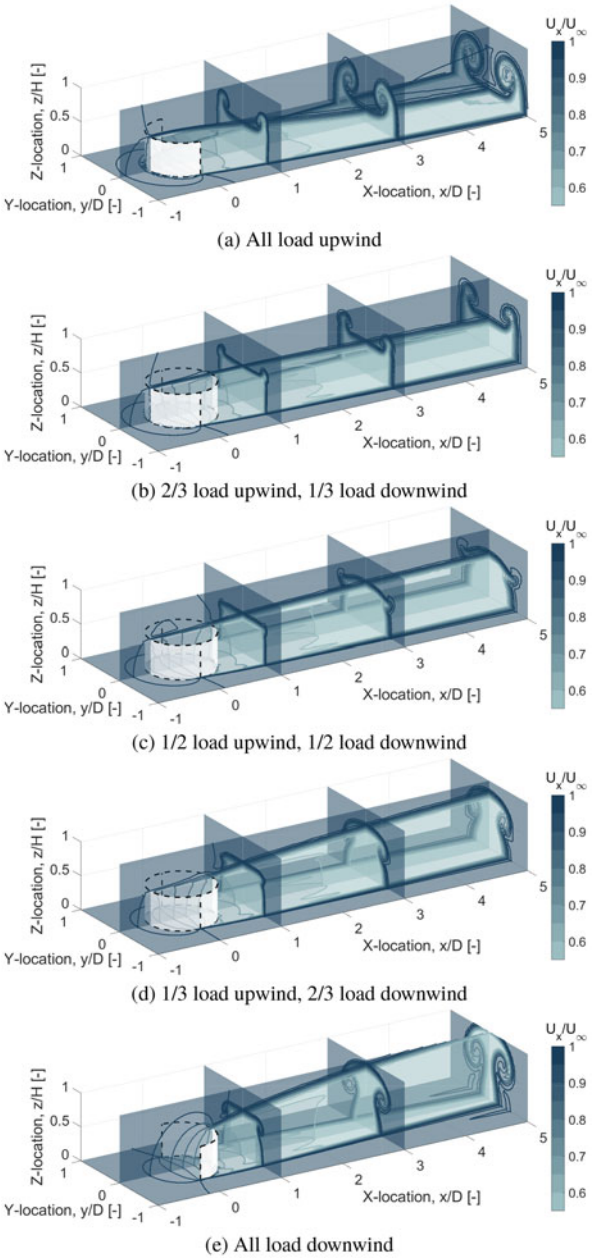

Fig. 21 X-velocity in the wake behind a 3D rotor with various load configurations. C_T is 0.67. H/D is 1. The loads are uniform and normal to the actuator. (a) All load upwind. (**b**) 2/3 load upwind, 1/3 load downwind. (**c**) 1/2 load upwind, 1/2 load downwind. (**d**) 1/3 load upwind, 2/3 load downwind. (**e**) All load downwind. (Adapted from De Tavernier et al. 2020b)

Horizontal Wake Deflection

Horizontal deflection uses the turbine blades to generate the lateral force needed to deflect the wake. As the wind can come from any direction, it is needed to control the direction of the wake. For any significant control, it is therefore necessary to have a pitch mechanism for the blades. One can make the distinction between having a constant pitch angle during the revolution, and varying the pitch angle during revolution. In the first case, one can change if the majority of the energy is extracted upwind or downwind. Except from the change between vertical and horizontal expansion as seen in Fig. 21, this will also generate a net lateral force as the tangential force has a different direction upwind vs downwind. The disadvantage of this concept will be that there is a limited range of pitch angles that can be used without losing too much blade performance, and risk stalling the blades, and the wake deflection will be low.

An active pitch angle can give significantly more control over the lateral force. With this technique, one can control the normal force to give a net force in one direction, and one can use the regions of the revolution when the relative wind angle is low to generate the lateral force, which can give a more significant wake deflection. The disadvantage is the need for active pitching throughout the revolution.

Vertical Wake Deflection

Vertical wake deflection is a technique proposed in Mendoza and Goude (2019). Here, it is proposed to use the struts to generate a vertical force. In principle, one can consider that the struts are designed to act as a fan blowing the air either up or down. The advantages of this method are that it does not require active pitching throughout the revolution. Also, it is less sensitive to the wind direction as the wind direction is mainly horizontal and a vertical deflection will cause the wake to avoid the downwind turbine independent of wind direction. The method can either be applied as a constant pitch, where the wake is always deflected, or with some kind of pitch mechanism or control surfaces for the struts to only deflect when needed. More studies are needed to determine which of these strategies that will yield the most cost-effective result.

An illustration of the technique is shown in Fig. 22, which is adapted from Mendoza and Goude (2019). The figure shows the wake 4 turbine diameters downstream a turbine with a square shaped cross section. In case wake deflection is applied (here generated by a 12 degrees pitch angle of the airfoil shaped struts), a significant part of the wake is located above the original cross section of the turbine. Figure 22c shows the power coefficient of both the first turbine (upwind) and the second turbine (located 6 diameters downwind from the first). The second turbine is in line with the first, or has a lateral offsets up to 1 turbine diameter from the first turbine (i.e., where the cross sections no longer overlap). The power coefficient is plotted against the pitch angle of the struts, where 0 refers to no wake deflection. This figure shows that the power loss from the first turbine is small, even for large deflections, while significant gain in power can be seen for the turbine directly

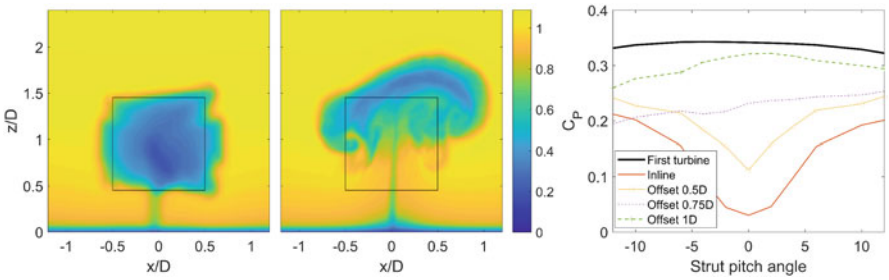

Fig. 22 Left and middle figures show the normalized flow velocity 4 diameters behind a turbine. The left without wake deflection and the middle with wake deflection through a 12 degree pitch angle on the struts. Black square represent the cross-sectional area of the turbine. Right figure shows the power of the first turbine, and powers of a second turbine 6D downwind, when turbine is inline, or offset from the first. (Adapted from Mendoza and Goude 2019)

behind the first. For the case with a 1 diameter offset a slight decrease is observed. The results here show promising results for a wake deflection technique based on very simple technology. One can expect that improved results should be achievable when the struts are optimized for wake deflection.

Airfoil Design for a VAWT

To improve the rotor performance of vertical-axis wind turbines, researchers have studied the effect of blade profiles intensively. In the early years of the VAWT history, researchers mainly opted for symmetric airfoils, notably the NACA 4-series (in particular the NACA 0012, NACA 0015, and NACA 0018), since it was believed important that the behavior was similar in the upwind and downwind part of the rotor, and because abundant information was available for symmetric airfoils. Later, pioneering research in the airfoil design for VAWTs has been performed at Sandia National Laboratories, Glasgow University, Tokai University, and Delft University of Technology, where new airfoils and design strategies are presented. At Sandia National Laboratories, Klimas (1992) investigated the desired characteristics of VAWT airfoils. He stated that modest maximum lift coefficients and sharp stall are important for stall regulation together with a low and wide drag bucket for unsteady effects. Around the 1980s, the University of Tokai (Kato et al. 1980) set a list of conditions for high aerodynamic efficiency, and they derived from simple streamtube models that a large lift gradient was important. Glasgow University (Galbraith et al. 1992) coupled an airfoil design optimization with a vorticity-based model of the rotor, eliminating many of the incorrect assumptions of streamtube models. More recently, at Delft University of Technology, Claessens (2006) designed airfoils for a small-scale rotor but contrary to earlier research a smooth stall behavior was preferred for noise reasons. Ferreira and Geurts (2015), Ferreira et al. (2015), and later De Tavernier et al. (2019) generated new

airfoils using a dual-objective genetic algorithm including an aerodynamic and structural optimization function. It is believed that it is necessary to balance the aerodynamic and structural efficiency in order to decrease the cost of energy of VAWTs. Furthermore, researchers such as Kirke (1998), Claessens (2006), Ferreira and Geurts (2015), and Ferreira and Geurts (2015) all agree that the sensitivity to roughness of the airfoils should be small.

Since the airfoil selection is of large importance in the VAWT design, this section is dedicated to this matter. Here we will focus on the aerodynamic objective function only.

As discussed in the previous sections, for a VAWT with infinite aspect ratio, the flow in the plane normal to the rotation axis is two-dimensional. If one considers a control volume that includes the rotor, the energy extracted or added to the flow is a function of the location and strength of the wake over the boundary of the control volume. According to Kelvin's theorem, the VAWT's wake is generated by the temporal/azimuthal variation of bound circulation on the blade. Its vorticity distribution is not dependent on the average bound circulation on the blade but only on its azimuthal variation. Implicitly, the same power conversion (same wake) can occur as the result of different loading distributions over Ferreira (2009), Ferreira and Scheurich (2014) and Madsen (1983) demonstrated that adding a constant bound circulation would, in 2D potential flow, have almost no net effect on the power conversion, but would result in a load shift between upwind and downwind regions of the rotation. The optimization of the energy conversion can be performed by optimizing the shedding of the wake. For a 2D VAWT defined by an actuator, the optimization of the wake generation implies the optimization of the curl of the load distribution over the surface, leaving a constant load distribution from the integral of the solution undetermined. An optimal loading distribution might in practice not be achievable or desired and therefore the question is: "What airfoil gives the most power converted into effective torque, for a given wake distribution or azimuthal variation of bound circulation?"

For a given number of blades and tip speed ratio, an azimuthal distribution of shed vorticity $\Gamma_{w(\theta)}$ implies a specific wake. This particular wake induces a specific velocity field, resulting in a specific azimuthal distribution of perceived velocity $V_{rel}\,(\theta)$ and inflow angle $\varphi\,(\theta)$. The distribution of shed vorticity $\Gamma_{w(\theta)}$ also implies a distribution of the gradient of the bound vorticity over the rotation $\mathrm{d}\Gamma_{\mathrm{b}}\,(\theta)\,/\mathrm{d}\theta$. We can define $\mathrm{d}\Gamma_{\mathrm{b}}(\theta)/\mathrm{d}\theta$ as $\mathrm{d}(\mathrm{C_l c V_{rel}})/\mathrm{d}\theta$.

Since, for a given wake, the local perceived velocity distribution $V_{rel}\,(\theta)$ is defined, a distribution of the time-derivative (or alternatively azimuth-derivative) of the bound vorticity over the rotation is equivalent to implying a distribution of $\mathrm{d}(\mathrm{C_l c})/\mathrm{d}\theta$. Although there is a unique distribution that satisfies the generation of the wake, there are an infinite number of suitable combinations of C_l and c that can be made. In the rotor design, these possible solutions can be achieved by, for example, adding a fixed pitch angle, changing the airfoil camber or other forms of circulation control. The average azimuthal distribution $\overline{c\cdot \mid C_{l_\theta} \mid}$ can be distinguished by the variation of the lift coefficient with the angle of attack and the variation of angle

of attack over the azimuthal position. The latter is defined by the velocity field, meaning that $\overline{|\ C_{l_\theta}\ |}$ is proportional to $\overline{|\ C_{l_\alpha}\ |}$.

Ideally, all extracted energy from the flow should be converted into mechanical power, that is, the torque T causing the turbine to rotate. However, this is limited by the effect of drag, as can be understood by Equation 71.

$$T = \int_0^{2\pi} R \cdot \frac{1}{2}\rho V_{rel}^2 c \left(C_l \sin(\phi) - C_d \cos(\phi)\right) d\theta \tag{71}$$

Assuming that the chord and velocity field are fixed (relative velocity V_{rel} =constant, inflow angle ϕ =constant, chord c =constant), which is a fair assumption for a fixed tip speed ratio case, the optimal circulation distribution is the one that corresponds to the optimal distribution of bound vorticity and at the same time minimizes drag throughout the rotation. The impact of the drag can be limited by minimizing the total $C_d c$ over the azimuthal positions. From this, the aerodynamic objective function on airfoil scale is derived and given in Equation 72.

$$\max\left[\frac{1}{\int_0^{2\pi} C_d c d\theta}\right] = \frac{1}{\text{const}} \cdot \max\left[\frac{\overline{|\ C_{l_\alpha}\ |}}{\int_0^{2\pi} C_d d\theta}\right] \qquad \text{where } \overline{c \cdot |\ C_{l_\alpha}\ |} = \text{const} \tag{72}$$

The final expression of the aerodynamic objective function is given in Equation 73 (Ferreira and Geurts 2015). The aerodynamic objective at rotor scale is to extract as much energy and approach optimal loading. On airfoil scale, this is translated to maximize the lift gradient over drag in the angle of attack range encountered by the rotor. The term $b(\alpha)$ represents a weighting function defining the occurrence of a certain angle of attack over one rotation. The domain in which the integral is evaluated is defined by a range of angle of attack $\Delta\alpha$ over which the turbine operates and a minimum angle of χ. χ can be varied from the minimum angle of attack for which the lift polar is given till the maximum angle of attack minus the angle of attack range, and can be understood as a fixed pitch.

$$f_{\text{aero}} = \max\left[\frac{\frac{1}{\Delta\alpha}\int_\chi^{\chi+\Delta\alpha} C_{l_\alpha} d\alpha}{\int_\chi^{\chi+\Delta\alpha} b(\alpha) \cdot C_d d\alpha}\right] \qquad \text{where } \alpha_{\min} < \chi < \alpha_{\max} - \Delta\alpha \tag{73}$$

Finally note that, because wind turbine blades often suffer from roughness due to dust, insect accumulation or surface damage, it is important to account for possible early turbulent transition in the aerodynamic objective function. For the full derivation, the reader is referred to Ferreira and Geurts (2015)

Cross-References

- Aerodynamics of Wake Steering
- Airfoil Design
- The Actuator Disc Concept

References

Adema N, Kloosterman M, Schepers G (2020) Development of a second-order dynamic stall model. Wind Energy Sci 5(2):577–590

Bachant P, Wosnik M (2015) Characterising the near-wake of a cross-flow turbine. J Turbul 16(4):392–410

Bangga G, Dessoky A, Lutz T, Krämer E (2019) Improved double-multiple-streamtube approach for H-Darrieus vertical axis wind turbine computations. Energy 182:673–688

Bangga G, Dessoky A, Wu Z, Rogowski K, Hansen MOL (2020a) Accuracy and consistency of cfd and engineering models for simulating vertical axis wind turbine loads. Energy 206:118087

Bangga G, Lutz T, Arnold M (2020b) An improved second-order dynamic stall model for wind turbine airfoils. Wind Energy Sci 5(3):1037–1058

Battisti L, Zanne L, Dell'Anna S, Dossena V, Persico G, Paradiso B (2011) Aerodynamic measurements on a vertical axis wind turbine in a large scale wind tunnel. J Energy Res Technol 133(3):031201

Beddoes TS (1987) A near wake dynamic model. In: Proceedings of the AHS national specialist meeting on aerodynamics and aeroacoustics

Borg M, Shires A, Collu M (2014) Offshore floating vertical axis wind turbines, dynamics modelling state of the art. Part I: aerodynamics. Renew Sustain Energy Rev 39:1214–1225

Cardona JL (1984) Flow curvature and dynamic stall simulated with an aerodynamic free-vortex model for VAWT. Wind Eng 9(3):135–143

Carr LW (1988) Progress in analysis and prediction of dynamic stall. J Aircraft 25(1):6–17

Chatelain P, Duponcheel M, Zeoli S, Buffin S, Caprace D-G, Winckelmans G, Bricteux L (2017) Investigation of the effect of inflow turbulence on vertical axis. J Phys Conf Ser 854:012011

Claessens MC (2006) The design and testing of airfoils for application in small vertical axis wind turbines. Msc thesis, Delft University of Technology

De Tavernier D (2021) Aerodynamic advances in Vertical-Axis Wind Turbines. PhD thesis, Delft University of Technology

De Tavernier D, Ferreira C (2019) An extended actuator cylinder model: actuator-in-actuator cylinder (AC-squared) model. Wind Energy 22:1058–1070

De Tavernier D, Ferreira C, Bussel G (2019) Airfoil optimisation for vertical axis wind turbines with variable pitch. Wind Energy 22(4):547–562

De Tavernier D, Sakib M, Griffith T, Pirrung G, Paulsen U, Madsen H, Keijer W, Ferreira C (2020a) Comparison of 3d aerodynamic models for vertical-axis wind turbines: H-rotor and phi-rotor. J Phys Conf Ser 1618:052041

De Tavernier D, Ferreira C, Paulsen U, Madsen H (2020b) The 3D effects of a vertical-axis wind turbine: rotor and wake induction. J Phys Conf Ser 1618:052040

Durand WF (1935) Aerodynamic theory – volume II division E general aerodynamic theory. Springer, Berlin

Dyachuk E, Goude A (2015) Simulating dynamic stall effects for vertical axis wind turbines applying a double multiple streamtube model. Energies 8(2):1353–1372

Ferreira CS (2009) The near wake of the VAWT. PhD thesis, Delft University of Technology

Ferreira CS, Geurts B (2015) Aerofoil optimization for vertical-axis wind turbines. Wind Energy 18(8):1371–1385

Ferreira CS, Scheurich F (2014) Demonstrating that power and instantaneous loads are decoupled in a vertical-axis wind turbine. Wind Energy 17(3):385–396
Ferreira CS, Madsen HA, Barone M, Roscher B, Deglaire P, Arduin I (2014) Comparison of aerodynamic models for vertical axis wind turbines. J Phys Conf Ser 524:012125
Ferreira CS, Barone MF, Zanon A, Kemp R, Giannattasio P (2015) Airfoil optimization for stall regulated vertical axis wind turbines. In: AIAA SciTech forum: 33rd wind energy symposium, (2015-0722)
Galbraith R, Coton F, Dachun J (1992) Aerodynamic design of vertical axis wind turbines. Report 9246, Glasgow University
Gormont RE (1973) A mathematical model of unsteady aerodynamics and radial flow for application to helicopter rotors. Report, Boeing Vertol
Goude A (2012) Fluid mechanics of vertical axis turbines – simulations and model development. PhD thesis, Uppsala University
Griffith DT, Paquette J, Barone M, Goupee AJ, Fowler MJ, Bull D, Owens B (2016) A study of rotor and platform design trade-offs for large-scale floating vertical axis wind turbines. J Phys Conf Ser 753:102003
Griffith DT, Barone M, Paquette J, Owens B, Bull D, Ferreira CS, Goupee A, Fowler M (2018) Design studies for deep-water floating offshore vertical axis wind turbines. Report SAND2018-7002, Sandia National Laboratories
Gross D, Harris FD (1969) Prediction of inflight stalled airloads from oscillating airfoil data. In: Proceedings of the 25th annual forum of the American helicopter society
Hansen MOL (2008) Aerodynamics of wind turbines, 2nd edn. Earthscan/Routledge, Chichester
Hara Y, Suzuki T, Ochiai Y, Hayashi T (2011) Velocity field measurements in wake of a straight-bladed vertical axis wind turbine
Hara Y, Kawamura T, Akimoto H, Tanaka K, Nakamura T, Mizumukai K (2014) Predicting double-blade vertical axis wind turbine performance by a quadruple-multiple streamtube model. Int J Fluid Mach Syst 7(1):16–27
Hirsch C, Mandal AC (1985) Flow curvature effect on vertical axis Darrieus wind turbine having high chord-radius ratio. In: Proceedings of the European wind energy conference, pp 405–410
Kato Y, Seki K, Shimizu Y (1980) Vertical axis wind turbine designed aerodynamically at Tokai university. Report, Tokai University
Katz J, Plotkin A (2001) Low speed aerodynamics, 2nd edn. Cambridge University Press, Cambridge
Kinzel M, Mulligan Q, Dabiri JO (2012) Energy exchange in an array of vertical-axis wind turbines. J Turbul 13:1–13
Kirke BK (1998) Evaluation of self-starting vertical axis wind turbines for stand-alone applications. PhD thesis, Griffith University
Klimas PC (1992) Tailored airfoils for vertical axis wind turbines. Report SAND84-1062, Sandia National Laboratories
Kumar PM, Sivalingam K, Lim T-C, Ramakrishna S, Wei H (2019) Review on the evolution of Darrieus vertical axis wind turbine: large wind turbines. Clean Technol 1(1):205–223
Leishman JG (2006) Principles of helicopter aerodynamics, vol 2. Cambridge university Press, Cambridge
Leishman JG, Beddoes T (1989) A semi-empirical model for dynamic stall. J Am Helicopter Soc 34(3):3–17
Li A (2017) Double actuator cylinder (AC) model of a tandem verticalaxis wind turbine (VAWT) counter-rotating rotor concept operating in different wind conditions. Msc thesis, Technical University of Denmark, Delft University of Technology
Madsen HA (1982) The Actuator Cylinder – a flow model for vertical axis wind turbines. The institute of industrial constructions and energy technology
Madsen HA (1983) On the ideal and real energy conversion in a straight bladed vertical axis wind turbine. PhD thesis, Aalborg University
Madsen HA (1985) Actuator cylinder: a flow model for vertical axis wind turbines. In: Proceedings of the BWEA wind energy conference (British Wind Energy Association), pp 147–154

Madsen HA, Larsen TJ, Vita L, Paulsen US (2013) Implementation of the Actuator Cylinder flow model in the HAWC2 code for aeroelastic simulations on vertical axis wind turbines. In: Proceedings of 51st AIAA aerospace sciences meeting including the new horizons forum and aerospace exposition, (2013-0913)

Mendoza V, Goude A (2019) Improving farm efficiency of interacting vertical-axis wind turbines through wake deflection using pitched struts. Wind Energy 22(4):538–546

Mendoza V, Chaudhari A, Goude A (2018) Performance and wake comparison of horizontal and vertical axis wind turbines under varying surface roughness conditions. Wind Energy 22(4):458–472

Migliore PG (1983) Comparison of NACA 6-series and 4-digit airfoils for Darrieus wind turbines. J Energy 7(4):291–292

Migliore PG, Wolfe WP, Fanucci JB (1980) Flow curvature effects on Darrieus turbine blade aerodynamics. J Energy 4(2):49–55

Möllerström E, Gipe P, Beurskens J, Ottermo F (2019) A historical review of vertical axis wind turbines rated 100 kw and above. Renew Sustain Energy Rev 105:1–13

Moran WA (1977) Giromill wind tunnel test and analysis. Report, U.S. Energy Research and Development Administration

Ning A (2016) Actuator Cylinder theory for multiple vertical axis wind turbines. Wind Energy Sci 1(2):327–340

Paraschivoiu I (1988) Double-multiple stream tube model for studying vertical-axis wind turbines. J Propuls Power 4(4):370

Paraschivoiu I (2002) Wind turbine design with emphasis on Darrieus. Polythecnic International Press, Montreal

Peng HY, Lam HF, Lee CF (2016) Investigation into the wake aerodynamics of a five-straight-bladed vertical axis wind turbine by wind tunnel tests. J Wind Eng Ind Aerodyn 155:23–35

Pirrung GR, Madsen HA, Kim T, Heinz J (2016) A coupled near and far wake model for wind turbine aerodynamics. Wind Energy 19(11):2053–2069

Pirrung GR, Riziotis V, Madsen HA, Hansen M, Kim T (2017a) Comparison of a coupled near- and far-wake model with a free-wake vortex code. Wind Energy Sci 2(1):15–33

Pirrung GR, Madsen HA, Schreck S (2017b) Trailed vorticity modeling for aeroelastic wind turbine simulations in standstill. Wind Energy Sci 2(2):521–532

Read S, Sharpe DJ (1980) An extended multiple streamtube theory for vertical axis wind turbines. In: Proceedings of the second BWEA wind energy workshop, pp 65–72

Rolin VFC, Porté-Agel F (2018) Experimental investigation of vertical-axis wind-turbine wakes in boundary layer flow. Renew Energy 118:1–13

Snel H (1997) Heuristic modelling of dynamic stall characteristics. In: Proceedings of European wind energy conference, pp 429–433

Strickland J (1975) The Darrieus turbine: a performance prediction model using multiple streamtubes. Report SAND75-041, Sandia National Laboratories

Strickland J, Smith T, Sun K (1981) Vortex model of the Darrieus turbine: an analytical and experimental study. Report SAND81-7071, SANDIA National Laboratories

Sutherland HJ, Berg DE, Ashwill TD (2012) A retrospective of VAWT technology. Report SAND2012-0304, Sandia National Laboratories

Templin R (1974) Aerodynamic performance theory for the NRC vertical-axis wind turbine. Report LTRLA-160, National Aeronautical Establishment Laboratory

Tescione G, Ragni D, He C, Ferreira CJS, van Bussel GJW (2014) Near wake flow analysis of a vertical axis wind turbine by stereoscopic particle image velocimetry. Renew Energy 70:47–61

Tran C, Petot D (1981) Semi-empirical model for the dynamic stall of airfoils in view of the application to the calculation of responses of a helicopter blade in forward flight. Vertica 5(1):35–53

Truong V (1993) A 2D dynamic stall model based on a hopf bifurcation. In: Proceedings of 19th European rotorcraft forum

Wilson R, Lissaman P (1974) Applied aerodynamics of wind powered machines. Report NSF-RAN-74-113, Oregon State University

Zanon A, Giannattasio P, Simão Ferreira CJ (2015) Wake modelling of a VAWT in dynamic stall: impact on the prediction of flow and induction fields. Wind Energy 18(11):1855–1874